




Geochemical fingerprinting of key lithologies and depositional processes across the upper boundary of the Opalinus Clay (Aalenian, Middle Jurassic, northern Switzerland)

Bruno Lauper¹  | Gaudenz Deplazes² | Hendrik Vogel³  | David Jaeggi⁴ |
Stephan Wohlwend⁵ | Daniel Ariztegui⁶  | Anneleen Foubert¹ 

¹Department of Geosciences, University of Fribourg, Fribourg, Switzerland

²Nagra, Wettingen, Switzerland

³Institute of Geological Sciences and Oeschger Centre for Climate Change Research, University of Bern, Bern, Switzerland

⁴Federal Office of Topography swisstopo, Wabern, Switzerland

⁵Geological Institute, ETH Zurich, Zürich, Switzerland

⁶Department of Earth Sciences, University of Geneva, Geneva, Switzerland

Correspondence

Bruno Lauper, Department of Geosciences, University of Fribourg, Fribourg, Switzerland.

Email: bruno.lauper@unifr.ch

Funding information

National Cooperative for the Disposal of Radioactive Waste (Nagra); Federal Office of Topography swisstopo

Abstract

The Opalinus Clay is an argillaceous to silty mudstone formation, notable in Switzerland as the selected host rock for deep geological disposal of radioactive waste. Its upper bounding unit (Passwang Formation and eastern equivalents) is composed of successions of mudstone, sandy bioclastic marl and limestone separated by ooidal ironstone beds. The lithostratigraphic transition is diachronous across northern Switzerland and shows high vertical and lateral lithological variability. To constrain this variability into predictive models, and to identify horizons with properties that could potentially influence radionuclide mobility, the sedimentological and diagenetic processes involved in the genesis of this transition have to be investigated. The present study aims at testing the applicability of X-ray fluorescence chemostratigraphy to characterise the mixed carbonate–siliciclastic units and understand the complex genesis of the lithostratigraphic transition from the Opalinus Clay towards its upper bounding unit. Sediment drill cores from four locations across northern Switzerland (Mont Terri, Riniken, Weiach and Benken) are analysed using high-resolution X-ray fluorescence core scanning. Data are compared to petrographic and additional geochemical data sets (inductively coupled plasma mass spectrometry, scanning electron microscopy with energy dispersive X-ray analysis, micro-X-ray fluorescence mapping) obtained from powdered samples, thin section analyses and drill core slabs. The results demonstrate that the combination of these rapid and non-destructive measurements along with multivariate data analysis allows the fast and objective classification of lithofacies along complex sedimentary successions. Moreover, it provides quantitative means for differentiating between prominent depositional and post-depositional processes. The lithostratigraphic transition has been traced by the use of specific elemental proxies as a discontinuity, and its genesis linked to sediment bypassing.

This is an open access article under the terms of the Creative Commons Attribution License, which permits use, distribution and reproduction in any medium, provided the original work is properly cited.

© 2020 The Authors. *The Depositional Record* published by John Wiley & Sons Ltd on behalf of International Association of Sedimentologists.

KEYWORDS

Mont Terri rock laboratory, mudstone, Murchisonae-Oolith Formation, ooidal ironstone, Passwang Formation, XRF core scanning

1 | INTRODUCTION

The Opalinus Clay is a mudstone succession with very low permeability (Nagra, 2002). This formation has been proposed as the potential host rock for radioactive waste disposal in Switzerland (Nagra, 2014). Since 1996, it has been intensively studied in the Mont Terri rock laboratory, an underground research facility situated in the Jura Mountains, in north-western Switzerland (Bossart *et al.*, 2017; Thury and Bossart, 1999). The Passwang Formation and the 'Murchisonae-Oolith Formation' are lithostratigraphic units overlying the Opalinus Clay and are composed of successions of mudstone, sandy bioclastic marl and limestone, separated by Fe-ooidal intervals (Bläsi *et al.*, 2013; Burkhalter, 1996; Hostettler *et al.*, 2017; Wohlwend *et al.*, 2019). This lithostratigraphic transition is diachronous across northern Switzerland and displays high vertical and lateral facies variability. In order to constrain this lithological variability into predictive models, and to identify horizons with properties that could potentially influence radionuclide mobility, it is essential to understand the different sedimentological and diagenetic processes involved in the formation of this transition.

X-ray fluorescence (XRF) core scanning, a non-destructive logging technique, provides continuous information on relative changes in elemental concentration at very high spatial resolution (down to 200 μm). Downcore variability in elemental data sets has successfully been applied to decipher variations in environmental, sedimentological and diagenetic processes (Bloemsmä *et al.*, 2012; Croudace and Rothwell, 2015; Cuvén *et al.*, 2010; Deplazes *et al.*, 2019; Jaccard *et al.*, 2005; Vogel *et al.*, 2010; among many others), and assist in correlation studies (Chatellier *et al.*, 2018; Kaboth-Bahr *et al.*, 2019; Thöle *et al.*, 2020).

The aim of the present study is: (a) to explore the applicability of XRF core scanning to differentiate between lithologies; (b) to characterise the depositional and post-depositional processes along a complex, mixed carbonate–siliciclastic lithostratigraphic transition; and (c) to understand better the sedimentary and geochemical processes that shaped the vertical and lateral variability at the lithostratigraphic boundary of the Opalinus Clay with its overlying units in four drill cores across northern Switzerland (Mont Terri, Riniken, Weiach and Benken).

2 | GEOLOGICAL SETTING

The Opalinus Clay and its upper bounding unit (Passwang Formation and eastern equivalents) were deposited during

late Toarcian to early Bajocian times in a shallow-marine epicontinental sea covering central Europe (Ziegler, 1990). At that time, central Europe was situated about 30° north of the equator (Irving, 1977). Considering that no major glaciation is known from the Jurassic, one can infer a subtropical to tropical climate (cf. Etter, 1990) with dense vegetation and lateritic soil formation on the continent (Burkhalter, 1995; Siehl and Thein, 1989; Young, 1989). While sediment provenance and palaeogeography remain unclear, it is suggested that the closest landmasses were situated at least tens to hundreds of kilometres away from the investigated sites (Etter, 1990; Wetzel and Allia, 2003). Situated at the southern end of the South German Basin, the Swiss northern basin was bordered by the Rhenish Massif to the north-west, by the Bohemian Massif to the east, by the Alemannic Islands to the south and by the Burgundy High to the west.

Although the Opalinus Clay has not yet been officially delineated by the Swiss Committee for Stratigraphy (Burkhalter and Heckendorn, 2009; Remane *et al.*, 2005), this informal lithostratigraphic unit has a long history in northern Switzerland (Quenstedt, 1843; 1858; Schmidt *et al.*, 1924). In Germany, on the other hand, the term Opalinuston Formation (Franz and Nitsch, 2009) is used and its upper limit is set within the Comptum Subzone (Opalinum Zone), at the base of the Comptumbank. A similar definition was used in northern Switzerland by Burkhalter (1996) to distinguish the Opalinus Clay from the overlying Passwang Formation. However, biostratigraphic studies have demonstrated that this lithological transition is diachronous across northern Switzerland, rendering its precise location and lateral correlation difficult. While the transition is attributed to the upper Opalinum Subzone (lower Opalinum Zone) in the Mont Terri area (north-western Switzerland; see Figure 1; Hostettler *et al.*, 2020), it is sometimes younger towards the east, typically formed during the Comptum Subzone to the Murchisonae Zone (Bläsi *et al.*, 2013; Feist-Burkhardt, 2012; Wohlwend *et al.*, 2019). The lithostratigraphic boundary between the Opalinus Clay and its upper bounding unit (henceforth abbreviated to OPA/UBU) is consequently not always straightforward to delineate. While in most locations the OPA/UBU boundary is marked by a conspicuous calcareous horizon (Bläsi, 1987; Burkhalter, 1996; Burkhalter *et al.*, 1997; Hostettler *et al.*, 2017; Matter *et al.*, 1987; 1988; Wohlwend *et al.*, 2019), some successions display gradual lithological changes with successive calcareous horizons (Frickberg; Wohlwend *et al.*, 2019). Hence,

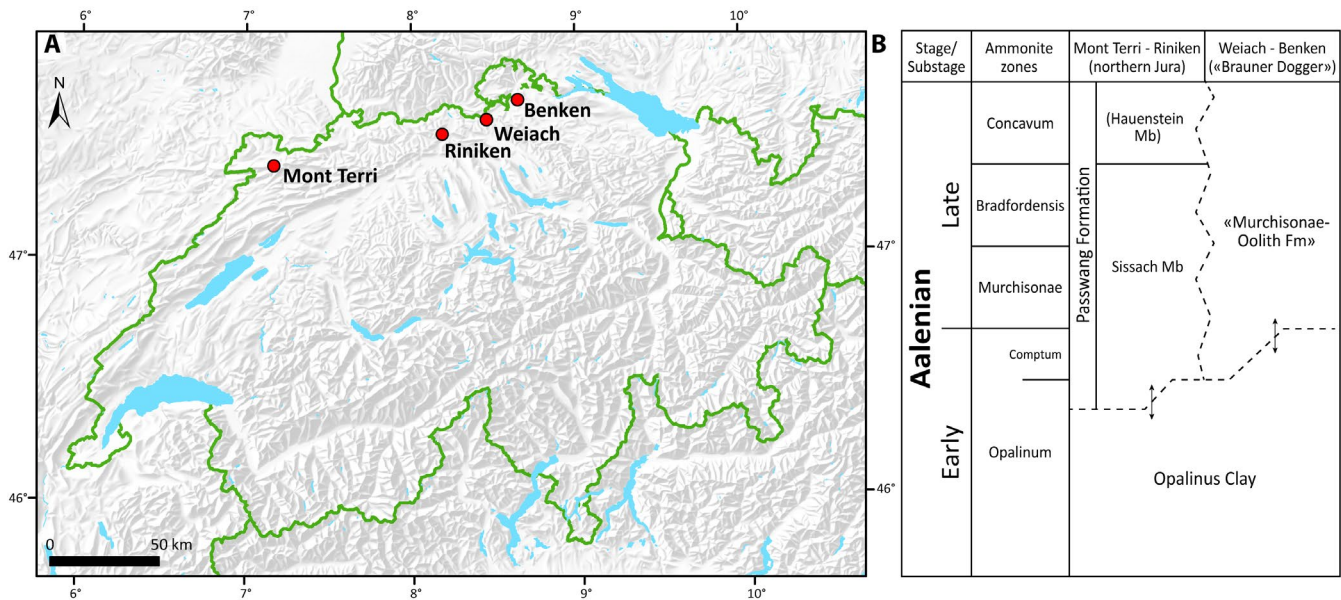


FIGURE 1 (A) Map of Switzerland and location of the studied drill cores. Source: Federal Office of Topography swisstopo. (B) Synthesis of the Aalenian stratigraphy in northern Switzerland (modified after Bläsi *et al.*, 2013; Wohlwend *et al.*, 2019). The boundary delineating the Opalinus Clay from its upper bounding unit fluctuates between the Opalinum and Murchisonae zones (see text for details). The Comptum Subzone constitutes the upper part of the Opalinum Zone, while its lower part is referred to as the Opalinum Subzone. Further subzones are not indicated. The Hauenstein Member (Burkhalter, 1996) is undifferentiated at Mont Terri (Hostettler *et al.*, 2017). 'Brauner Dogger' refers to Bläsi *et al.* (2013). Fm = Formation; Mb = Member

within the Benken drill core, the position of the OPA/UBU boundary was reallocated after new biostratigraphic data were acquired (Bläsi *et al.*, 2013; Feist-Burkhardt, 2012).

The 80–130 m thick Opalinus Clay is present in the Swiss Jura and Molasse Basin, as well as in Germany. It is an argillaceous to silty mudstone, which is composed of clay minerals (kaolinite, illite-smectite mixed layers, illite and chlorite), quartz (mainly coarse silt to fine sand) and carbonates (mostly calcite, some siderite, dolomite and ankerite) in varying concentrations. Some minor and accessory components include pyrite, K-feldspar, plagioclase, biotite, muscovite, rutile, zircon, apatite, monazite, glauconite and organic matter (Peters, 1962; Pearson *et al.*, 2003; Lerouge *et al.*, 2014; see Mazurek, 2011 for an overview of the existing mineralogical database). The Opalinus Clay lithology varies regionally. In the Mont Terri area, the formation is divided into five lithostratigraphic sub-units, characterised by three lithofacies: the shaly facies, the carbonate-rich sandy facies and the sandy facies (Bossart and Thury, 2008; Hostettler *et al.*, 2017; Lauper *et al.*, 2018). Further east, the Opalinus Clay is typically divided into five to six sub-units, tentatively correlatable across the area (Bläsi, 1987; Matter *et al.*, 1987; 1988; Nagra, 2001). A lithostratigraphic overview of the Opalinus Clay across northern Switzerland is provided by Nagra (2002) and Mazurek and Aschwanden (2020). Detailed lithofacies and subfacies descriptions and interpretations are provided by Wetzel and Allia (2003) and Lauper *et al.* (2018).

In the northern Swiss Jura, the Opalinus Clay is overlain by the Passwang Formation. Originally defined as an alloformation, it is characterised by parasequences of mudstone, sandy bioclastic marl and limestone, separated by ooidal ironstone beds (Burkhalter, 1996). Strong regional variations in lithology and facies distribution occur. East of the Jura (eastwards from the Aare River), the 'Murchisonae-Oolith Formation', the Wedelsandstein Formation and the 'Humphriesioolith Formation' (as defined by Bläsi *et al.*, 2013 and references therein) are time-equivalents of the Passwang Formation. In the Mont Terri area, the basal Passwang Formation, the so-called Sissach Member, shows a thin intraclastic, Fe-ooidal horizon followed by sandy marl and bioclastic limestone (Hostettler *et al.*, 2017). In the eastern Jura, the basal Passwang Formation forms four different lithofacies, varying mainly between spathic, sandy marl and limestone, and Fe-ooidal ironstone (Wohlwend *et al.*, 2019). Further east, the 'Murchisonae-Oolith Formation' shows a Fe-ooidal horizon followed by sandy marl with bioclastic limestone intervals (Bläsi *et al.*, 2013; Burkhalter *et al.*, 1997).

The complex lithostratigraphic and biostratigraphic framework of the OPA/UBU transition is typically attributed to differential subsidence (Bläsi *et al.*, 2013; Wohlwend *et al.*, 2019). During the Lower Jurassic, an extensive stress field caused by the opening of the Tethys and the Atlantic Ocean induced the reactivation of pre-existing basement structures (Permo-Carboniferous troughs; Reisdorf and Wetzel, 2018;

Wetzel *et al.*, 2003; Wildi *et al.*, 1989). The rifting was associated with the formation of fault bounded tilted blocks, which led to a series of local basins by differential subsidence. The resulting depositional area was morphologically differentiated into swells and depressions, contributing significantly to the lateral facies variability (Burkhalter, 1996; Lauper *et al.*, 2018; Wetzel and Allia, 2000; 2003; Wetzel and Meyer, 2006).

3 | MATERIALS AND METHODS

Drill core sections crossing the OPA/UBU lithostratigraphic transition at four different locations were investigated: (a) 2.90 m from the Mont Terri rock laboratory (BPE-3 core; depth interval 11.45 to 14.35 drilling m; see Gygax *et al.*, 2017); (b) 5.09 m from Riniken (Nagra well; depth interval 330.06–335.15 m; see Matter *et al.*, 1987); (c) 2.64 m from Weiach (Nagra well; depth interval 553.16–555.80 m; see Matter *et al.*, 1988); and (d) 1.42 m from Benken (Nagra well; depth interval 539.00–540.42 m; see Nagra, 2001; see Bläsi *et al.*, 2013 for updated lithostratigraphy). Table 1 provides an overview of the investigated material and analyses. Core locations are indicated on Figure 1.

3.1 | Sedimentary petrography

The petrography and mineralogy of the Opalinus Clay and its upper bounding unit is documented in several reports and publications (Bläsi, 1987; Burkhalter, 1995; 1996; Franz and Nitsch, 2009; Kneucker *et al.*, 2020; Lauper

et al., 2018; Lerouge *et al.*, 2014; Matter *et al.*, 1987; 1988; Mazurek, 2011; Mazurek and Aschwanden, 2020; Nagra, 2001; 2002; Wetzel and Allia, 2003; Wohlwend *et al.*, 2019). Additionally, new petrographic analyses of selected drill core sections were performed at macro-scale and micro-scale. For drill cores acquired more than 30 years ago (Riniken and Weiach), pictures taken shortly after coring were compared to new facies observations to evaluate post-drilling alteration. Existing thin sections from the Riniken, Weiach and Benken drill cores (Nagra internal collection; respectively Matter *et al.*, 1987; 1988; Nagra, 2001), as well as thin sections from a drill core crossing the Mont Terri rock laboratory (BDB-1; Reisdorf *et al.*, 2016) were used for microfacies descriptions. Most of the thin sections were stained with potassium ferricyanide and alkaline red S in acid solution (Dickson, 1965). Additional polished thin sections were retrieved from the BPE-2 core (Mont Terri, drill core close to BPE-3; Gygax *et al.*, 2017) and from the Riniken core. Thin sections were studied by classical petrographic microscopy (Leica DM4500 P; Leica). Additional observations, analyses and elemental mapping of selected samples from the Riniken core were performed with a FEI XL30 Sirion FEG (Thermo Fisher Scientific) scanning electron microscope (SEM) coupled with an Energy Dispersive Spectrometer (EDX; X-Max 150 Silicon Drift Detector; Oxford Instruments) at 20 kV (Department of Geosciences, University of Fribourg). Prior to analyses, a thin carbon layer was sputter-coated on the samples.

Siliciclastic-dominated lithologies are described following Lazar *et al.* (2015), while bedding structures (lenticular and flaser) refer to Reineck and Wunderlich (1968). Carbonate-dominated lithologies are described using the

TABLE 1 Overview of investigated material, respectively borehole information, references and applied analyses

Borehole	BPE-3 (Mont Terri)	Riniken (Nagra)	Weiach-1 (Nagra)	Benken (Nagra)
Location (WGS84)	Mont Terri rock laboratory; 47°22'41.750"N 7°10'1.531"E ^a	47°30'16.225"N 8°11'23.770"E	47°33'49.636"N 8°27'30.267"E	47°38'41.695"N 8°38'58.371"E
Borehole orientation	About 57° towards bedding	Perpendicular to bedding	Perpendicular to bedding	Perpendicular to bedding
Borehole total length (m)	26.70	1,800.50 m	2,482.00 m	1,007.00 m
Original report references	Gygax <i>et al.</i> (2017)	Matter <i>et al.</i> (1987)	Matter <i>et al.</i> (1988)	Nagra (2001)
Studied depth interval (m)	11.45–14.35	330.06–335.15	553.16–555.80	539.00–540.42
Available material	Stained TS from BDB-1	Stained TS; 1 cm thick slab of OPA/UBU transition	Stained TS	Stained TS
New material	Polished TS from BPE-2	Polished TS	—	—
Analyses	Petr.; XRF-CS	Petr.; XRF-CS; μ -XRF; ICP-MS; SEM-EDX	Petr.; XRF-CS	Petr.; XRF-CS

Abbreviations: Petr., petrography; TS, thin sections.

^aCoordinates from BPE-3 borehole are approximate.

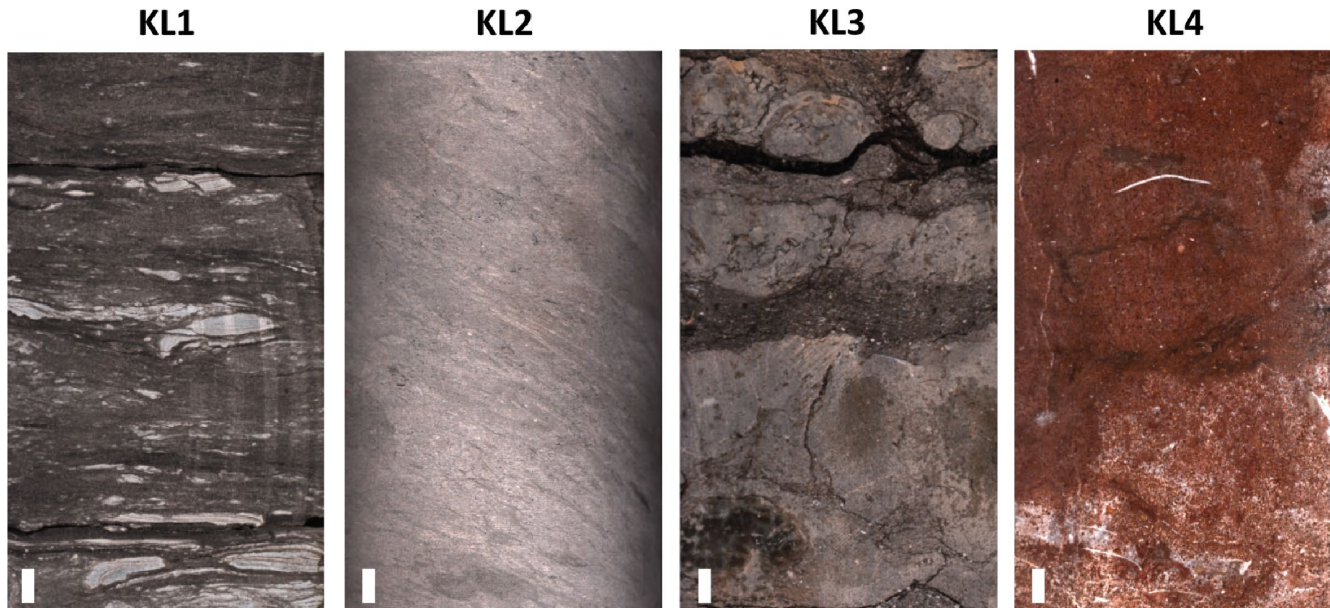


FIGURE 2 Representative sections of the key lithologies. KL1: argillaceous to argillaceous–siliceous mudstone (Opalinus Clay interval at Riniken). KL2: siliceous–calcareous sandstone to sandy bioclastic packstone/grainstone (basal Passwang Formation at Mont Terri; cross-bedding drilled at 57° angle). KL3: bioclastic sandy wackestone to packstone (lower part of the Weiach OPA/UBU-delineating horizon). KL4 ooidal ironstone (basal Passwang Formation at Riniken). Scale bar is 1 cm

Dunham (1962) classification. Iron-rich rocks are described as ironstones (abnormally high iron content), following the terms and glossary summarised by Young (1989).

3.2 | X-ray fluorescence core scanning

Elemental intensities were measured using an ITRAX XRF core scanner (Cox Analytical Systems) at the University of Bern (see Croudace *et al.*, 2006 for details on the ITRAX core scanner). Different measurement settings (current and voltage) were applied, while exposure time was constantly set at 50 s.

Measurements were performed at 10 mm intervals in relatively homogeneous sediments and at 5 mm in more heterogeneous material (mostly carbonate) for all cores, except the Benken sections, which were measured at 5 mm intervals throughout all lithologies.

The BPE-3 whole-round core sections from Mont Terri were measured with a Mo-tube at 30 kV and 40 mA. The Riniken archive split-core sections were measured with a Mo-tube set to 30 kV and 50 mA, and with a Cr-tube set to 30 kV and 50 mA. The Weiach archive split-core sections were measured with a Mo-tube set to 30 kV and 40 mA. The Benken whole-round core sections (except the OPA/UBU interval that was split; 539.72–539.52 m) were measured with a Cr-tube set to 30 kV and 50 mA.

Raw X-ray fluorescence core scanning (XRF-CS) spectra were processed in the software Q-spec (version 8.6.0). Standard adjustment and refinement of the peak-fitting parameters using representative parts of the core sections was

performed. Outliers corresponding to structural defaults were subsequently removed.

3.3 | XRF-CS data analysis

Resulting downcore variations of selected elements are presented as ratios of element-intensity counts normalised to Al. Aluminium is assumed to be exclusively of detrital origin, a good representative of the clay fraction, and shows a conservative behaviour throughout changing redox conditions (Calvert and Pedersen, 2007; Löwenmark *et al.*, 2011).

To investigate the relationship between elemental content across the different lithologies, principle component analysis (PCA) was performed on each data set using the freely available PAST software (Hammer *et al.*, 2001). Detailed information on PCA is provided by Wold *et al.* (1987). Considering the compositional nature of elemental data, a centred log-ratio (clr) transformation was applied to the whole XRF-CS data sets prior to element selection and PCA (Aitchison, 1986; Bloemsmas *et al.*, 2012). Biplots were used to determine the type of relationship between selected elements and to visualise their differing trends among distinct lithostratigraphic/lithological units.

3.4 | Micro X-ray fluorescence mapping

In order to characterise chemical diversity among the mineralogical, textural and structural phases, three representative areas (different sizes, a few tens of cm²) were mapped along a 1 cm

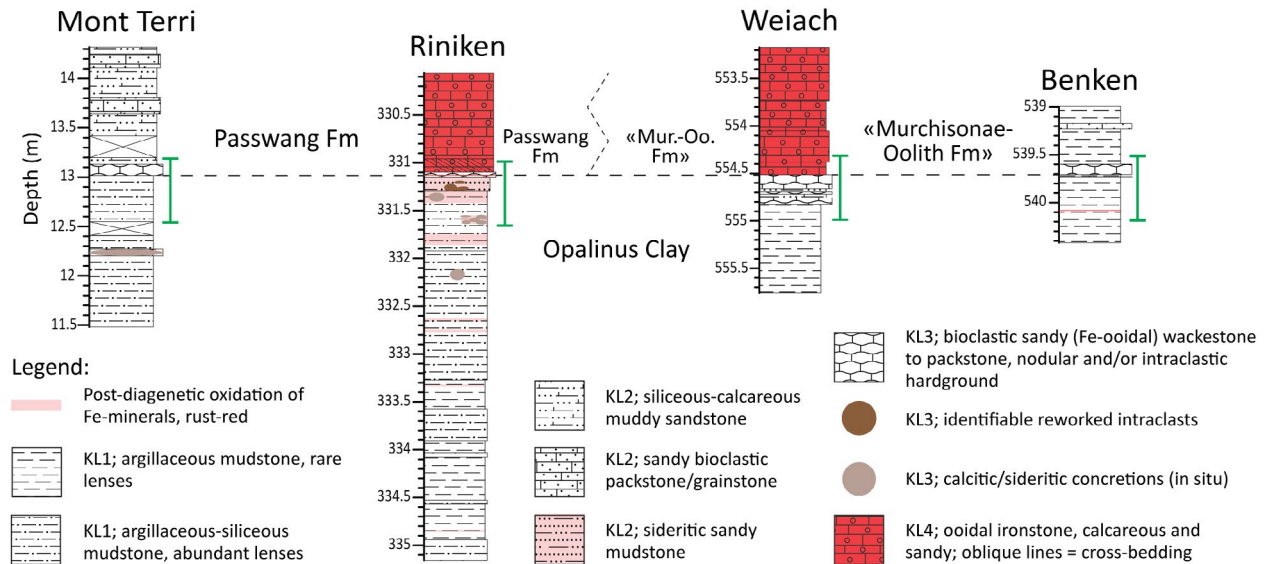


FIGURE 3 Lithological logs of the studied drill core sections. Dashline indicates the defined OPA/UBU lithostratigraphic boundary based on Matter *et al.* (1987; 1988), Bläsi *et al.* (2013) and Hostettler *et al.* (2017). The green brackets indicate the areas illustrated in Figure 4. Fm = Formation; 'Mur.-Oo. Fm' = 'Murchisonae-Oolith Formation'. Ooidal ironstone (basal Passwang Formation at Riniken). Scale bar is 1 cm

thick slab representing the OPA/UBU transition in the Riniken core sections. Micro-XRF mapping was performed at ultra-high resolution (detector spot size = 50 μm) with the Eagle III micro X-ray fluorescence ($\mu\text{-XRF}$) spectrometer (Röntgenanalytik Messtechnik GmbH) at the University of Geneva. Current settings were set at 40 kV and 400 mA, and integration time at 10 μs .

3.5 | Inductively coupled plasma mass spectrometry

Two vertically adjacent sub-samples of 8 cm³ of bulk rock were taken from 10 spots along the Riniken core sections (see Figure S1) and ground in an agate mortar. Major and

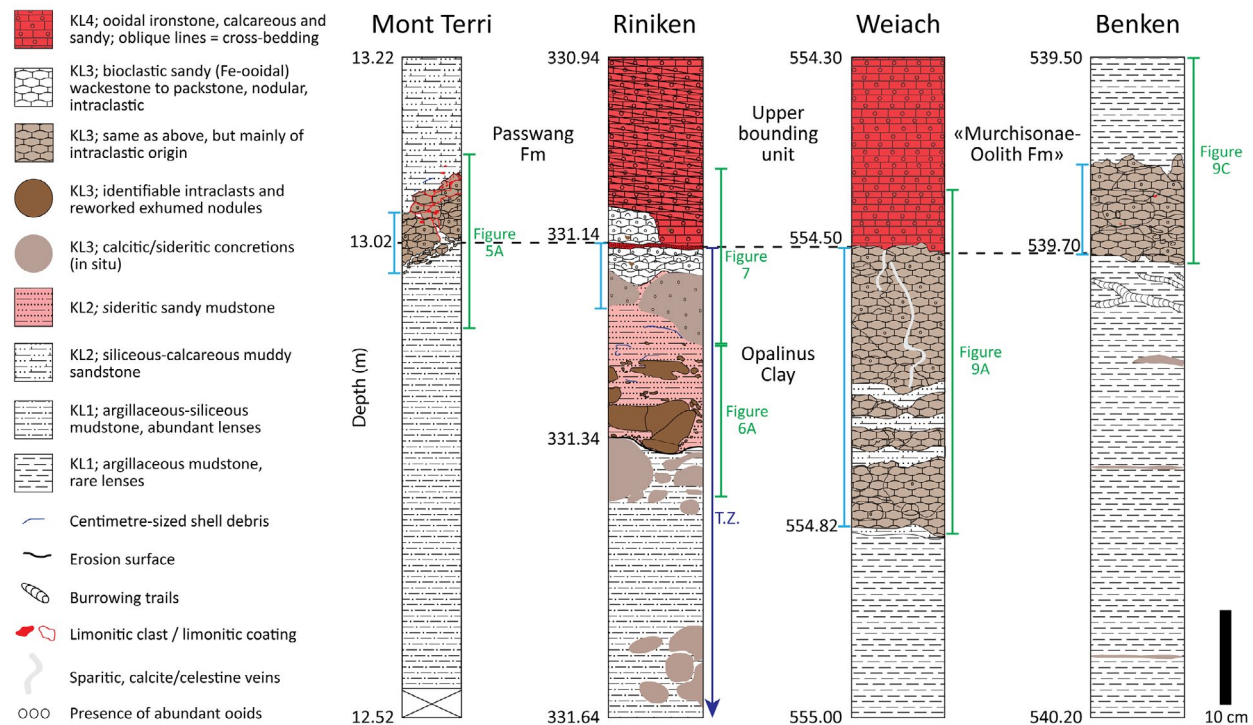


FIGURE 4 Lithological detail of the OPA/UBU transitional intervals. The studied Mont Terri drill core has a smaller diameter than the Nagra drill cores, and was not drilled perpendicular to bedding. The light blue brackets identify the OPA/UBU-delineating horizons. The dark blue arrow points to the illustrated part of the Transition Zone (T.Z.; Riniken). The green brackets indicate the areas illustrated in Figures 5A, 6A, 7 and 9A,C. Fm = Formation

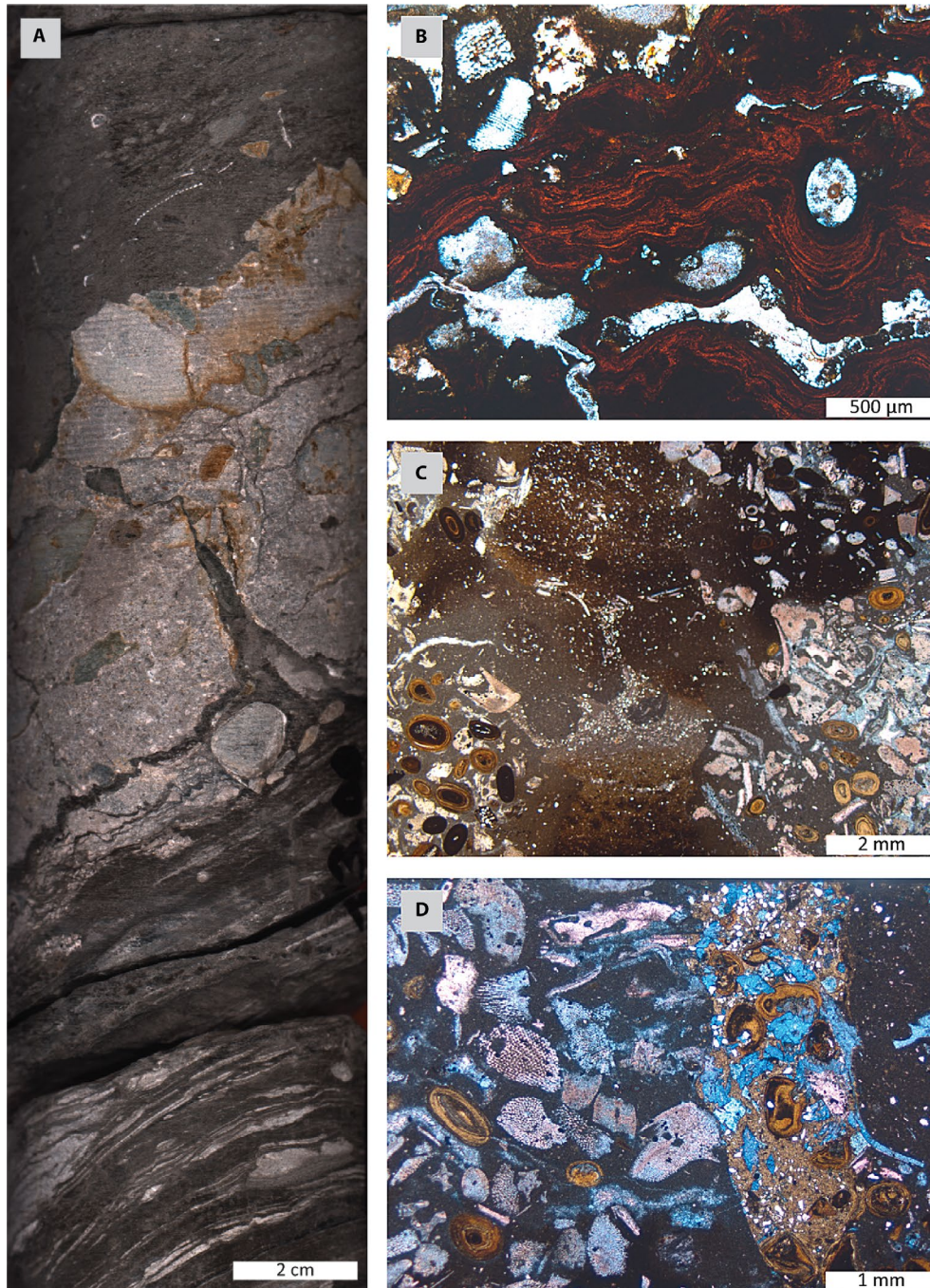
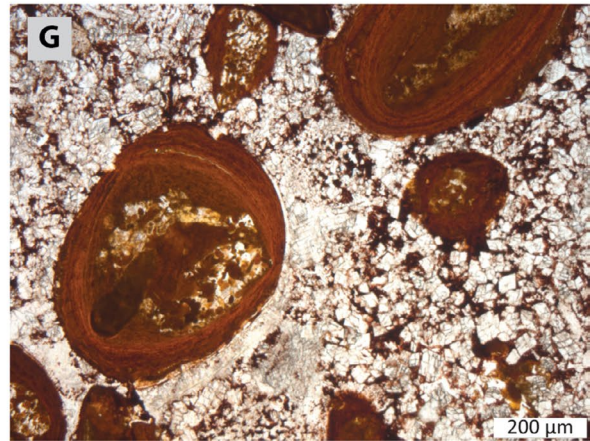
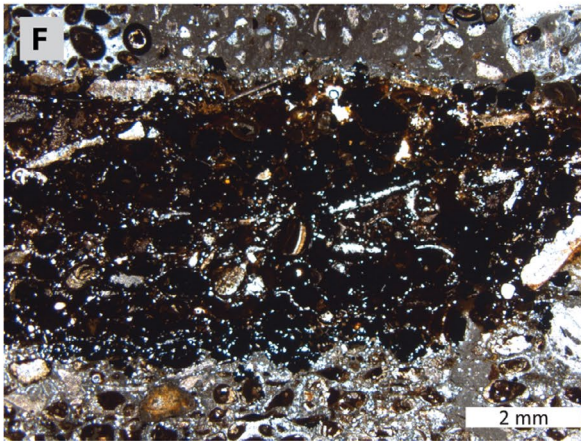
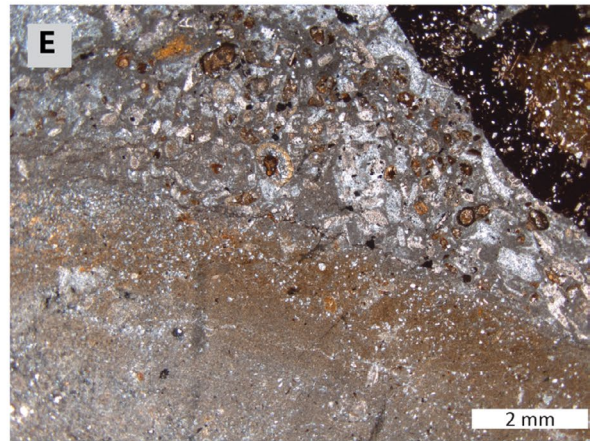
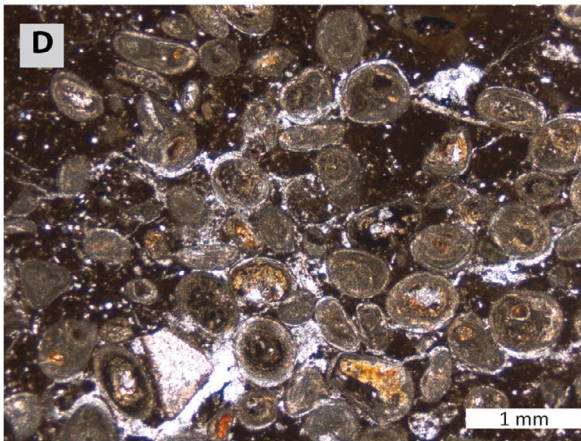
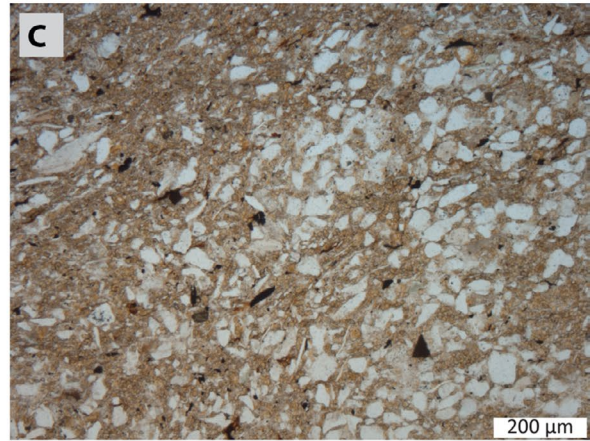
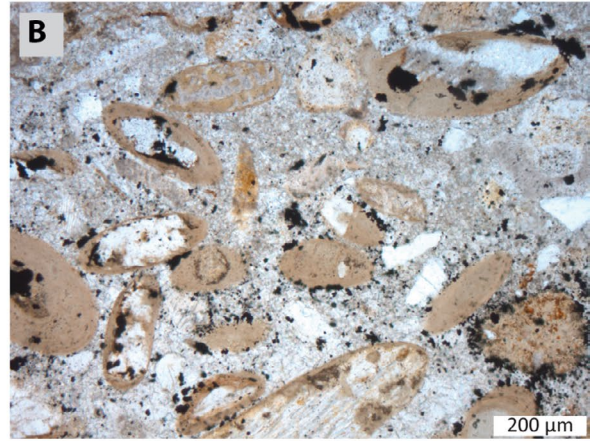
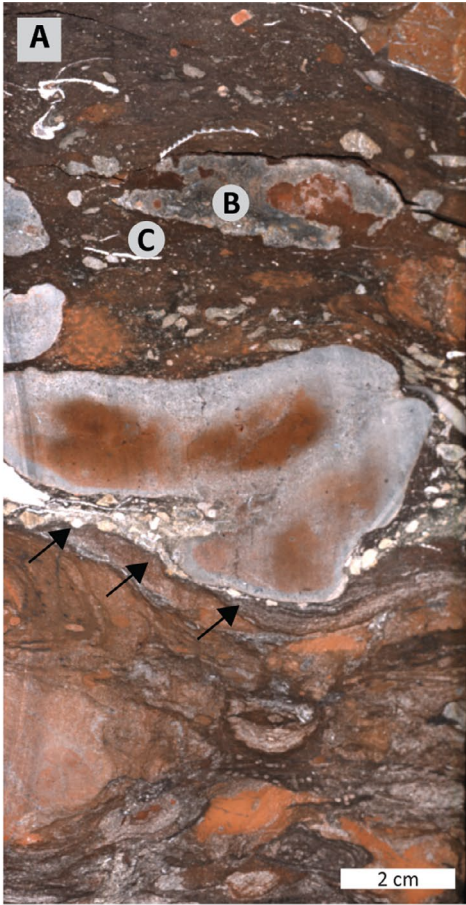


FIGURE 5 Hardground at Mont Terri. (A) Macroscopic view of the hardground delineating the OPA/UBU lithostratigraphic boundary within the BPE-3 drill core. The OPA/UBU-delineating horizon is attributed to the Passwang Formation (Hostettler *et al.*, 2017). Smaller clasts occur at the base, while ferruginous microbialites occur mainly within the upper part. (B) Photomicrograph of ferruginous microbialites with mammilated texture occurring within the upper part of the hardground (from a neighbouring drill core; BPE-2). (C) Typical lithology of the hardground. Fe-ooids, bioclasts and quartz grains occur within a bioturbated, ferruginous, micritic matrix. Right side of the photomicrograph is stained (from BPE-2). (D) Stained photomicrograph showing a boring filled with Fe-spastoliths (plastically deformed Fe-ooids) and fine-grained material (from BPE-2). All photomicrographs were acquired in plane-polarised light

trace element abundances of the resulting 20 samples were analysed by inductively coupled plasma mass spectrometry (ICP-MS) through a commercial laboratory (Actlabs; package Code Ultratrace 7). Prior to analysis, samples were fused with sodium peroxide in a zirconium crucible

and acidified with concentrated nitric and hydrochloric acids. The resulting solutions were diluted and analysed by an Agilent 7900 ICP-MS (Agilent Technologies). Calibration was performed using five synthetic calibration standards.



4 | RESULTS

4.1 | Lithology

4.1.1 | Key lithologies along the OPA/UBU transition

Four key lithologies (KL) are observed along the studied successions (Figure 2).

Lithofacies KL1 consists of an argillaceous to argillaceous-siliceous mudstone. Occasional to abundant millimetre to centimetre-thick lenses occur within a fine-grained and clay-rich matrix (lenticular bedding). Only a few lenses are continuous over the overall core diameter. They are composed of silt to fine-sand quartz grains and bioclastic debris (mainly mollusc shell and echinoderm fragments). The grains are mostly cemented by Fe-rich calcite. A few pyrite framboids occur throughout the matrix and lenses. This lithology is characteristic of the investigated Opalinus Clay intervals.

Lithofacies KL2 consists of a siliceous-calcareous sandstone to sandy bioclastic packstone/grainstone. Abundant fine-sand quartz grains are mixed with bioclastic fragments (mainly echinoderms and mollusc shells). A few iron-coated grains, dolomite crystals and pyrite framboids occur. The proportion of quartz and bioclasts varies along the core sections. This lithology is typical of the basal Passwang Formation at Mont Terri.

Lithofacies KL3 consists of a bioclastic sandy wackestone to packstone. This lithology is highly heterogeneous and includes calcitic/sideritic nodules and calcareous hardgrounds with frequent intraclasts. Some intraclasts contain iron-coated grains (including Fe-ooids) and ferruginous microbialites. Individual Fe-ooids also occur. Quartz grains are abundant in certain horizons, and heavy minerals such as zircon, monazite and rutile may be present. Pyrite and siderite represent significant components within certain horizons. This lithology typically forms the OPA/UBU-delineating horizons, but is not limited to them.

Lithofacies KL4 consists of an ooidal ironstone. This lithology is characterised by a rust-red colour primarily attributed to the abundant Fe-ooids and limonitic components. The Fe-ooids

are mostly spherical or ellipsoidal and less than 2 mm in diameter. Some Fe-pisoids, Fe-oncoids and Fe-spastoliths are also present, although all are named as Fe-ooids henceforth. Their mineralogy was not investigated within this study but is heterogeneous and dominated by goethite and chamosite (Burkhalter, 1995; 1996; Hostettler *et al.*, 2017). The limonitised bioclastic fragments and Fe-ooids typically occur within a dominantly sparitic matrix (calcite and dolomite). Some intervals show an important amount of Fe-rich and Al-rich clay minerals. Quartz silt-sized to sand-sized grains are also present in varying quantities. Pyrite is rare to absent. This lithology is typical of the Passwang Formation interval at Riniken and the 'Murchisonae-Oolith Formation' interval at Weiach.

4.1.2 | Sedimentary petrography

Figure 3 summarises the lithology of the four studied core intervals, and Figure 4 shows an expanded view of the lithological variability along the OPA/UBU transitions, such as defined by Matter *et al.* (1987; 1988), Bläsi *et al.* (2013) and Hostettler *et al.* (2017).

1.2.1 | Mont Terri

From stratigraphic base to top (11.48–14.32 drilling m), the BPE-3 core sections display first the upper sandy facies of the Mont Terri Opalinus Clay (11.48–13.02 m; Bossart and Thury, 2008; in this study described as KL1). Thin planar to slightly wavy lenses occur within an argillaceous matrix. They primarily represent starved ripples, but some bioturbation (round burrows) is also visible. A homogeneous micritic bed (mudstone/wackestone; probably a nodule at larger scale; see Hostettler *et al.*, 2020) is observed between 12.21 and 12.26 m.

The OPA/UBU lithostratigraphic boundary is sharp and characterised by an 8–11 cm thick, calcareous hardground (herein referred to as the OPA/UBU-delineating horizon). This horizon is composed of merged and jointly compacted, reworked Fe-ooidal and bioclast-rich intraclasts (wackestone/packstone) and exhumed biomicritic nodules (KL3; Figures 4 and 5A). Stylolitic-like structures are visible and extend over several centimetres. The edges of the

FIGURE 6 Lithological features from the Riniken core. (A) The erosive surface within the Transition Zone (uppermost Opalinus Clay) in the Riniken core is indicated by black arrows. The lower part shows in-situ calcitic/sideritic nodules forming a firm ground at the top of an argillaceous-siliceous mudstone facies. Above the erosive surface, biolith and lithoclastic intraclasts are present within a quartz-rich, sideritic muddy matrix. (B) Photomicrograph of Fe-ooidal intraclasts (see location in A). (C) Photomicrograph of the ferruginous quartz-rich matrix (see location in A). (D) Calcareous neomorphosed ooids from the uppermost nodular calcareous layer at the top of the sideritic condensed interval (Transition Zone in the Riniken core, below layer 'a'; see Figure 7). (E) Photomicrograph displaying the interface between two calcareous layers at the top of the Transition Zone in the Riniken core (OPA/UBU-delineating horizon). The lower layer ('a' in Figure 7) consists of a sandy wackestone and the upper layer ('b' in Figure 7) consists of a bioclastic packstone. (F) Photomicrograph of the >1 cm pyritised Fe-ooidal layer delineating the OPA/UBU lithostratigraphic boundary at Riniken. (G) Photomicrograph of the typical lithology of the basal Passwang Formation at Riniken. Fe-ooids occur within a calcitic, dolomitic and limonitic matrix. All photomicrographs were acquired in plane-polarised light

uppermost lithoclasts are encrusted by ferruginous microbialites with a stromatolitic texture (Figure 5B). Scarce to abundant bioclasts (mainly echinoderms, mollusc shell debris and foraminifers), common Fe-ooids, limonite-coated clasts, quartz silt grains and euhedral pyrite are present. Bioturbation features and boring traces are identified throughout this horizon (Figure 5C,D).

According to Hostettler *et al.* (2017), the OPA/UBU-delineating horizon defines the base of the Passwang Formation. Siliceous-calcareous sandstone alternating with 10–15 cm thick sandy bioclastic (many echinoderm fragments) packstone/grainstone intervals containing centimetres-thick veins and flaser structures (KL2; 13.11–14.32 m) are deposited on top of the hardground.

1.2.2 | Riniken

From stratigraphic base to top (335.15–330.06 m), the studied core sections display about 4 m of Opalinus Clay (335.15–331.14 m). The lower part (335.15–331.90 m) is characterised by a lenticular mudstone facies (KL1). Intervals with abundant and thick lenses alternate with intervals with rare and thin lenses. Some of the thicker lenses display current ripples. The level of bioturbation is medium to high, characterised by disrupted intervals and frequent burrows (rounded lenses) throughout the matrix. At a few locations, the lenticular structures are impregnated by rust-red Fe-oxides suggesting post-diagenetic alteration of Fe-minerals.

The upper part of the Opalinus Clay (331.90–331.14 m) is heterogeneous and differs from the underlying lithology. This heterogeneous interval is referred to as the Transition Zone. It contains comparatively more bioclastic remains and bioturbation has resulted in greater homogeneity. Distinct biomicrotic, calcitic/sideritic, rounded nodules occur (mudstone to wackestone). The deformation of the surrounding silty lenses indicates that sediment compaction occurred after nodule formation (i.e. at 331.56 and 332.15 m). At 331.34 m, an erosional surface occurs (Figure 6A). It is overlain by exhumed biomicrotic (calcitic/sideritic) nodules, reworked biolithitic and lithoclastic intraclasts, and shell fragments of several centimetres embedded within a quartz-rich, sideritic, muddy matrix (Figure 6A–C). Its uppermost part (331.20–331.14 m) is formed by a carbonate-rich, hardground unit (Figure 7; OPA/UBU-delineating horizon) characterised at the base by merged, in-situ, sideritic concretions containing neomorphosed (diagenetically altered) calcitic ooids, quartz grains and bioclastic fragments (shell debris, echinoderms, coral fragments; Figures 6D and 7). On top of it, distinct calcareous layers, a few centimetres thick, are present. They successively consist of (Figure 7): (a) sandy wackestone (Figure 6E); (b) bioclastic packstone with common Fe-spastoliths and partly neomorphosed Fe-ooids (Figure 6E); and (c) sandy, bioclastic, Fe-ooidal grainstone.

The latter ends within a <1 cm thick layer composed almost exclusively of Fe-ooids, some of which are fully pyritised (d; Figure 6F). Above this layer follows the Passwang Formation (from 331.14 m onwards; cf. Matter *et al.*, 1987; Burkhalter, 1995).

The basal Passwang Formation (331.14–330.06 m) displays a rust-red coloured ooidal ironstone typical of KL4. The lower part is characterised by a 20 cm thick cross-bedded interval followed by a more bioturbated section. Highly dolomitised (possibly ankerite) intervals occur (Figures 6G and 8). Quartz grains are common to abundant, and bioclasts consist mostly of echinoderm and mollusc shell fragments. Recrystallised ammonite and belemnite remains are observed.

1.2.3 | Weiach

From stratigraphic base to top (555.80–553.16 m), the core sections display an argillaceous mudstone facies (KL1; 555.80–554.50 m) characteristic of the Opalinus Clay. Only rare quartz/bioclast-rich lenses occur. At the time the core sections were inspected for this study, white post-diagenetic gypsum precipitation was observed around artificial desiccation cracks at the core surface. This alteration feature is associated with the dehydration caused by prolonged core storage.

The OPA/UBU lithostratigraphic boundary is characterised by a 32 cm thick, calcareous unit (OPA/UBU-delineating horizon; 554.82–554.50 m; Figures 4 and 9A). It is vertically heterogeneous and limestone beds alternate with muddy sandstone layers. The limestone beds consist of bioclastic, sandy, Fe-ooidal packstone to grainstone (KL3). Bioclasts include mainly mollusc shells, echinoderms and bryozoans. Limonitic components are abundant, but only a few show concentric structures typical of Fe-ooids. Some well-defined, millimetre to over 7 cm-sized intraclasts occur, a few of which are dolomitic. Stylolites are visible within the whole interval. Three 23 cm thick, interbedded muddy sandstone layers are present between the limestone beds. Parts of the overall OPA/UBU-delineating horizon display post-diagenetic precipitation of brownish Ca-sulphate minerals (Figure 9A). Furthermore, a calcite sparitic vein containing disseminated patches of fibrous celestine (identified by comparing with Lerouge *et al.*, 2014 and Mazurek and de Haller, 2017; no mineralogical data available; Figure 9A,B) occurs perpendicularly to the bedding within the upper part of the interval. According to Matter *et al.* (1988), this interval represents the stratigraphical top hardground of the Opalinus Clay.

From 554.50 to 553.16 m, the 'Murchisonae-Oolith Formation' displays a rust-red coloured ooidal ironstone (KL4). It is rich in quartz sand, bioclastic debris (mainly echinoderms and mollusc shell fragments) and Fe-coated (limonitic) grains (including true Fe-ooids). Few intraclasts

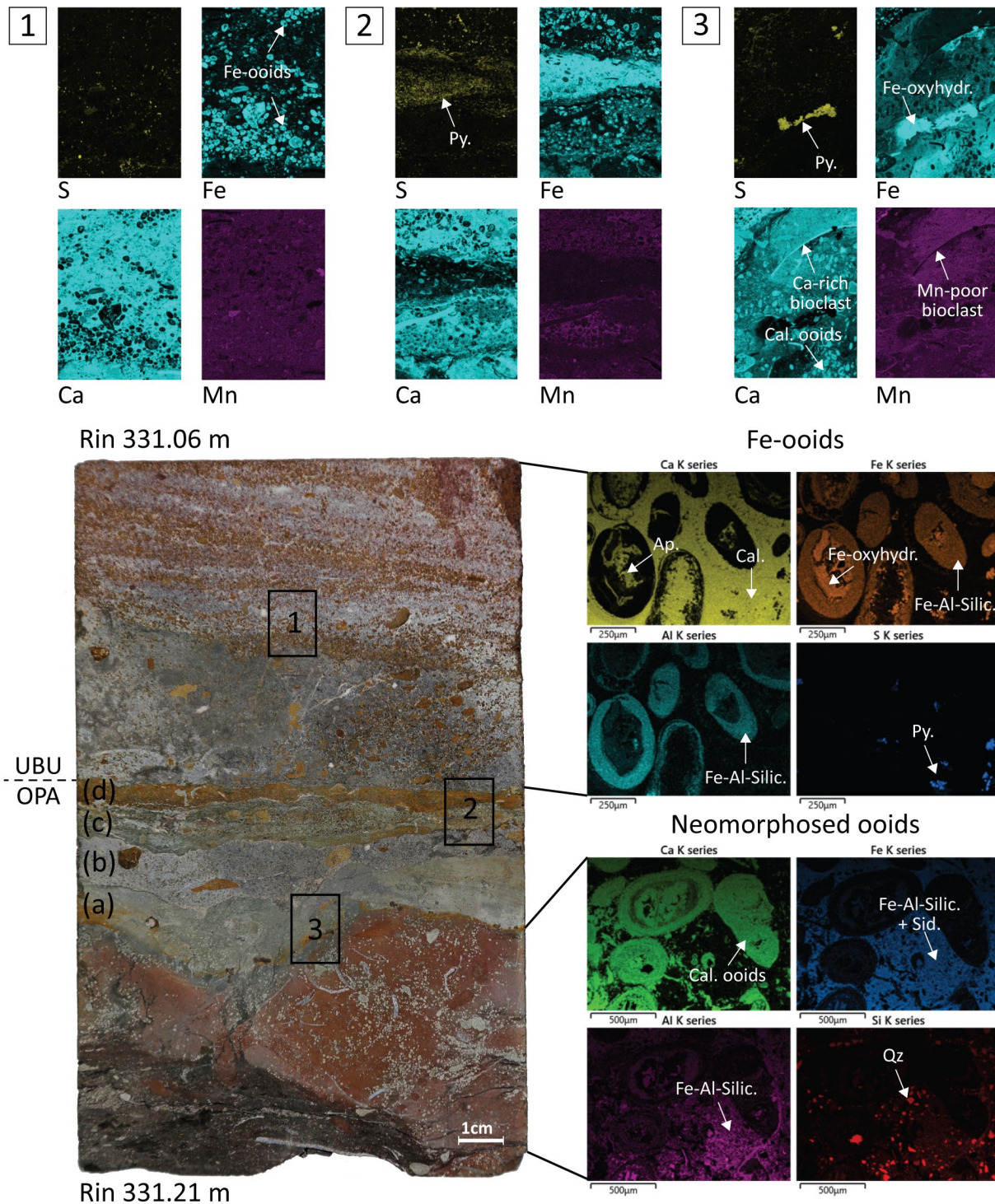


FIGURE 7 Photograph of the Riniken slab. The thin calcareous and Fe-oidal layers topping the Opalinus Clay are referenced by letters (a, b, c and d; see text for descriptions). The numbers display the location of the μ -XRF scans (upper part of the figure). SEM-EDX images, on the right side, display the elemental mapping of neomorphosed ooids at the bottom of the slab (Opalinus Clay), and Fe-rich ooids at the top of the slab (Passwang Formation). Ap. = apatite; Cal. = calcite; Fe-Al-Silic. = ferruginous and aluminous silicates (e.g. chamosite, kaolinite); Fe-oxyhydr. = iron oxyhydroxides; Py. = pyrite; Qz = quartz; Sid. = siderite

occur. Some parts show more Fe-rich and Al-rich clay minerals. The matrix is mainly sparitic and consists of calcite and dolomite (possibly ankerite) crystals. This overall facies is highly bioturbated.

1.2.4 | Benken

From stratigraphic base to top (540.42–539.00 m), the core sections display an argillaceous mudstone facies (KL1; 542–539.70 m) characteristic of the Opalinus Clay.

Riniken (Passwang Formation)

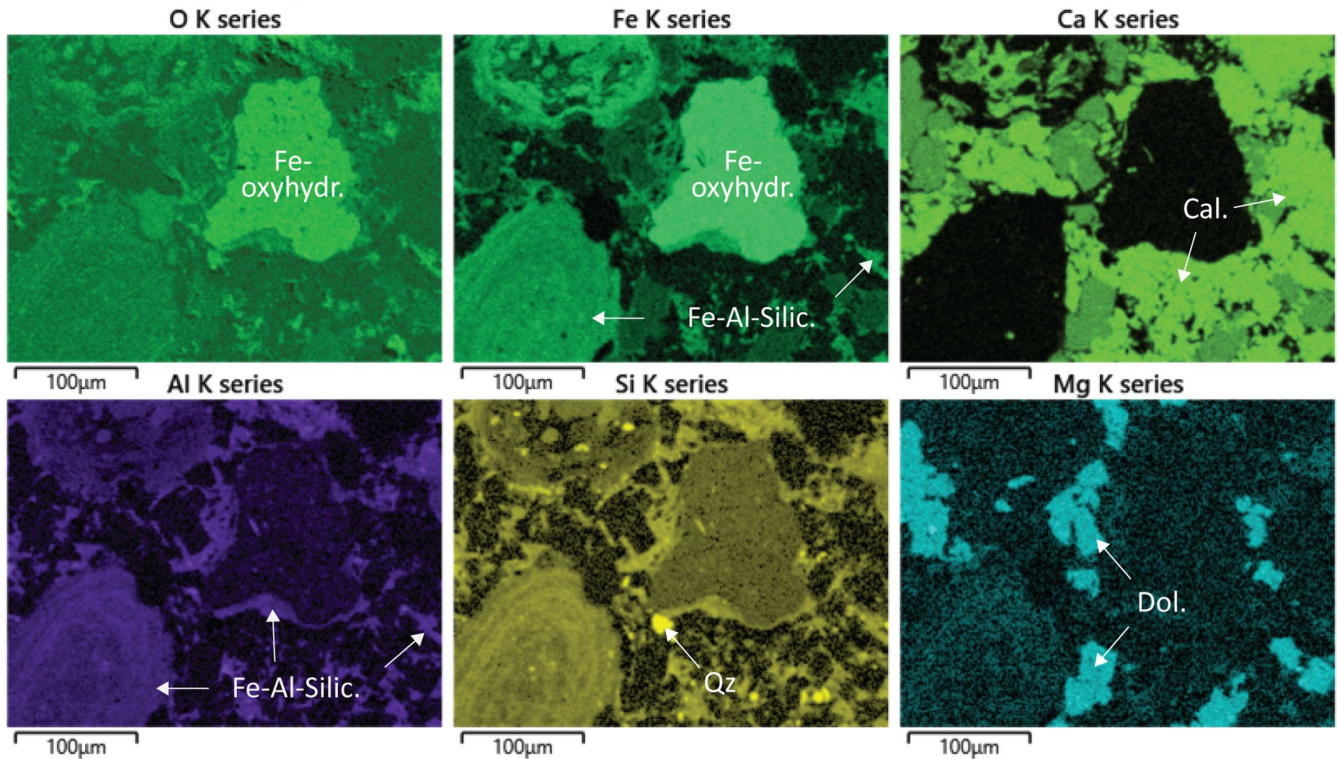


FIGURE 8 SEM-EDX images from the Passwang Formation at Riniken (KL4) displaying intensities of selected elements. Mineralogical composition of the components can be inferred. Cal. = calcite; Dol. = dolomite; Fe-Al-Silic. = ferruginous and aluminous silicates (e.g. chamosite, kaolinite); Fe-oxyhydr. = iron oxyhydroxides

Quartz-rich lenses are rare, but a few thin elongated sideritic layers occur. At 539.74 m, near-horizontal burrow traces filled with coarse silty quartz grains and bioclastic debris are visible.

The OPA/UBU lithostratigraphic boundary is sharp and characterised by a 10 cm thick, calcareous hardground (OPA/UBU-delineating horizon; KL3; 539.70–539.60 m; Figures 4 and 9C). This horizon is highly heterogeneous. It consists of bioclastic packstone with frequent, partly amalgamated biolithic and lithoclastic intraclasts. Bioclasts are generally abundant and of various origins (mollusc shells, echinoderms, foraminifers, bryozoans, etc.). Some intraclasts exhibit abundant neomorphosed calcitic ooids (Figure 9D), but no original goethitic/chamositic Fe-ooids were observed in thin section. Limonitic lithoclasts are however visible. Pyrite is abundant within certain intraclasts, while others show high siderite content. Quartz grains commonly occur. Styolitic structures extending over several centimetres are visible.

According to Bläsi *et al.* (2013), the OPA/UBU-delineating horizon forms the basal layer of the 'Murchisonae-Oolith Formation'. It is overlain by an argillaceous mudstone resembling the Opalinus Clay facies (KL1), albeit with a possibly higher carbonate content (539.60–539.00 m). A sharply delineated sandy bioclastic bed (KL2) occurs between 539.24 and 539.18 m.

4.2 | Sedimentary geochemistry

4.2.1 | Element concentrations: calibration and reliability of XRF-CS data

According to ICP-MS results from Riniken, the averaged major elements constituting the overall lithology are: Si (16.84%), Ca (13.68%), Fe (6.76%), Al (4.54%), S (1.36%), K (1.14%), Mg (1.00%) and Ti (0.30%), with strong differences depending on key lithologies. The remaining elements show values up to a maximum of a few hundred parts per million on average, with Mn as the highest minor element (*ca* 780 ppm on average). The ICP-MS results for all detectable elements can be found in Table S1.

The sampling methodology for ICP-MS measurements does not allow for direct comparison with XRF-CS data and cannot therefore serve for robust calibration, principally because of the heterogeneity of the sampled bulk volumes. It is particularly true for elements showing high lateral variability. Nevertheless, the most abundant elements show noteworthy and reliable correlations supporting the relative trends in the XRF-CS data (Figure 10). Rigorous quantification of absolute values is not required within the scope of the present study; the relative trends are sufficient for chemostratigraphic purposes, unravelling major lithological

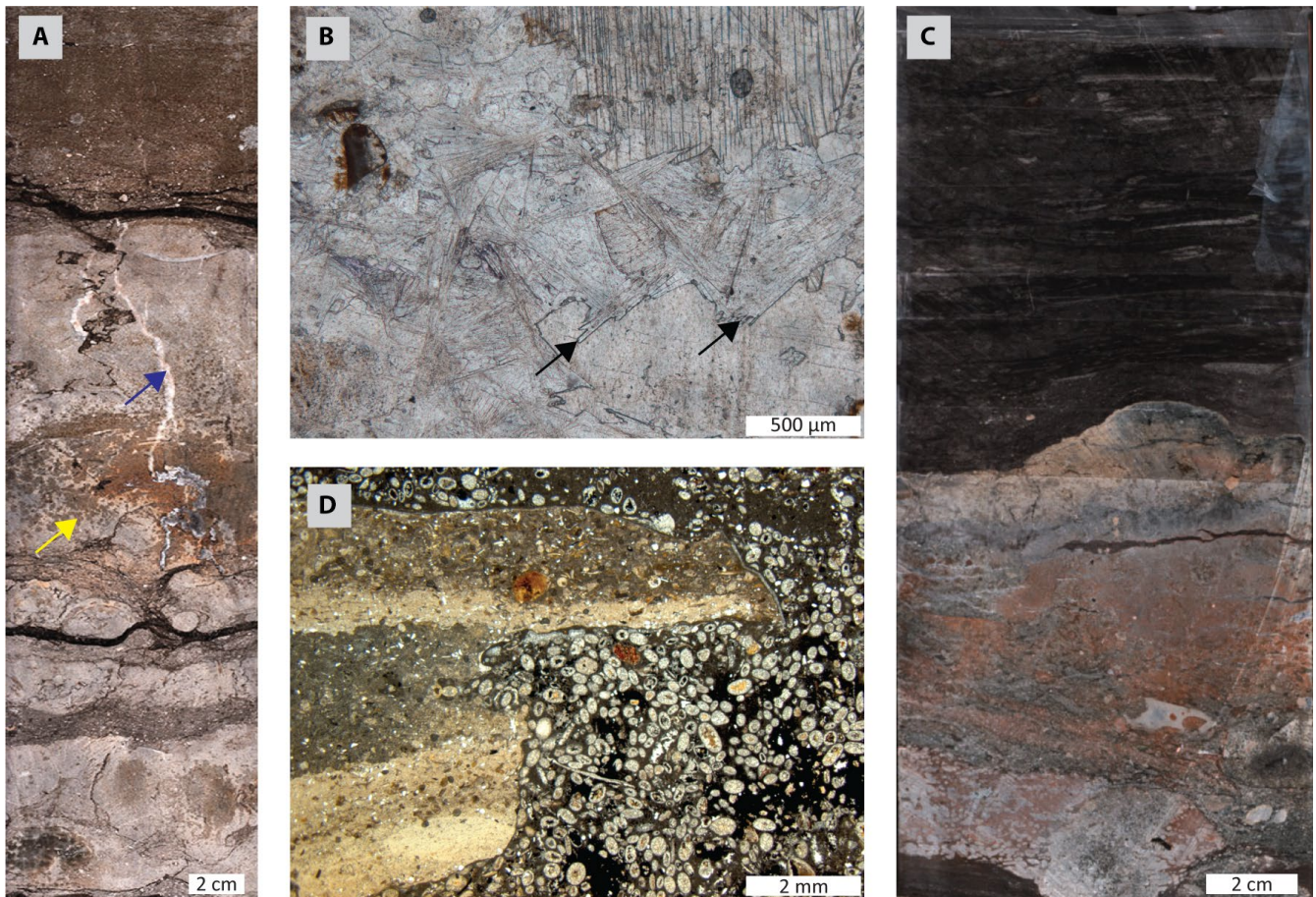


FIGURE 9 Lithological features from the Weiach and Benken cores. (A) The OPA/UBU transition at Weiach. The lower part consists of the OPA/UBU-delineating horizon (KL3), while the upper part illustrates the beginning of the limonitic lithology of the basal 'Murchisonae-Oolith Formation' (KL4). The calcitic vein with fibrous celestine is indicated by a blue arrow. Yellow arrow shows post-diagenetic alteration, probably Ca-sulphates. (B) Photomicrograph of a calcite/celestine vein from the OPA/UBU-delineating horizon at Weiach. Black arrows point to the fibrous celestine crystals. (C) The OPA/UBU transition at Benken. The lower part displays the OPA/UBU-delineating horizon (KL3), while the upper part illustrates the overlying argillaceous (-calcareous) mudstone of the 'Murchisonae-Oolith Formation' (KL1). (D) Photomicrograph from the OPA/UBU-delineating horizon in the Benken core. Calcitic neomorphosed ooids occur next to an intraclast within a ferruginous matrix. All photomicrographs were acquired in plane-polarised light

boundaries, and to disentangle key depositional and diagenetic processes.

Comparisons between elemental variations measured with the Mo-tube and the Cr-tube in the Riniken core support the reliability of the XRF-CS data sets. Correlation coefficients are higher than 0.75 for all major elements (not provided for Mg; see Table S2).

4.2.2 | Downcore elemental variations and lithological associations

Downcore variations of selected element ratios are displayed in Figures 11 and 12 as a function of core depth for all studied core intervals. The combination of different element ratios allows the following three chemofacies to be identified: (a) siliciclastic, (b) calcareous and (c) ferruginous.

The siliciclastic chemofacies is typically associated with KL1 and partly with KL2. This chemofacies shows a relative enrichment in terrigenous elements, such as Al, Si, K, Ti and Zr. These elements have a negative correlation with the carbonate fraction (Ca; Figure 13A). They are primarily present as building blocks or substituted within the clay minerals, mica, feldspar and quartz lattices. The elements correlate well (Figures 13B,C,D and 14), although small differences exist between them. The occurrence of thin silty/sandy lenses within a predominantly argillaceous matrix, such as within the Opalinus Clay mudstone facies (KL1), is expressed in comparatively higher Si/Al values, which are attributed to the higher quartz over clay minerals content. Hence, within a given lithology, (i.e. KL1 and KL2), the Si/Al ratio along with the Zr/Al ratio may be used to identify subtle grain-size variations (see also Calvert and Pedersen, 2007). Good correlations between Si and Zr are also evident in biplots and

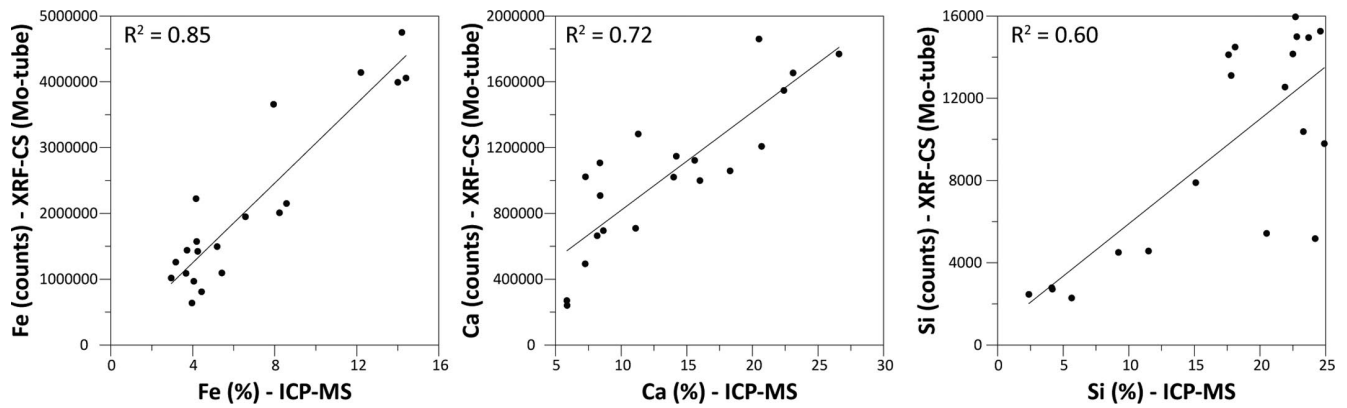


FIGURE 10 Biplots and correlation coefficients of selected elements measured by ICP-MS (%) versus XRF-CS (in total counts, with the Mo-tube), respectively

PCA (Figures 13D and 14) for the Mont Terri and Benken successions, both of which are predominantly composed of siliciclastic sediments. In contrast, the Riniken and Weiach successions are more heterogeneous, and the Al and Zr contents depend mostly on mineralogical composition rather than grain size. Within this chemofacies, Fe/Al, Mn/Al and S/Al are generally low (except at Weiach, where S/Al is high due to alteration products; see below) and correlates positively with the fine siliciclastic fraction. The good correlation between Fe/Al and S/Al within the Opalinus Clay mudstone facies at Mont Terri points to dispersed pyrite framboids (Figure 13E). A few striking peaks may occur, typically when pyritic (Fe/Al and S/Al peaks) or sideritic (Fe/Al and Mn/Al peaks) concretions are present (see e.g. KL1 in Benken sediments). In the Weiach core, relatively high and well-correlated Ca/Al and S/Al signals are recorded along the overall Opalinus Clay mudstone facies (KL1). Their relative enrichment and tight correlation (see Figure 13F) is atypical of the siliciclastic chemofacies and reflects rather the presence of gypsum encrustations on the core surface, disturbing the primary depositional signal of the mudstone facies.

The calcareous chemofacies is identified by the occurrence of dispersed carbonate nodules (KL3; see Mont Terri and Riniken), calcareous hardgrounds (KL3; OPA/UBU-delineating horizons in all studied successions) and spathic limestone beds (KL2; e.g. the Passwang Formation at Mont Terri). This chemofacies is evidence of a significant increase in Ca. While the Ca/Al ratio acts as the main proxy for all types of carbonates (bioclastic and authigenic/diagenetic), the data suggest that strong Mn enrichment supplements the Ca peaks within carbonates of diagenetic origin (nodules and cements). This assumption is supported by μ -XRF mapping displaying high Mn counts within calcite cement and authigenic phases, whereas bioclasts show low Mn intensities (Figure 7). Hence, the two spathic limestone beds within the Passwang Formation at Mont Terri display a significantly lower Mn increase in contrast to the strong Ca increase observed within these two intervals (Figure 15).

Where carbonate intervals are enriched in siderite (e.g. nodules within the Riniken Transition Zone), in Fe-hydroxides and Fe-silicates (typically within Fe-oids) or in pyrite (e.g. pyritised burrow at Benken), the Fe-related ratios display high values. Pyrite-rich intervals are supplemented by a significant S/Al increase, as pyrite is the main S-bearing phase within the Opalinus Clay (Pearson *et al.*, 2003). Other S-carriers include the late-diagenetic Ba-Sr-sulphates (fibrous celestine; Lerouge *et al.*, 2014; Mazurek and de Haller, 2017), such as identified in the OPA/UBU-delineating horizon at Weiach. The fibrous celestine is nevertheless very limited in extent (restricted to a vein) and displays significant Ba and Sr peaks, although not illustrated within the framework of this study. Interestingly, the OPA/UBU-delineating horizons are associated with higher Zr values compared to other terrigenous elements (Figures 11 and 12). The Mont Terri and Benken successions exhibit Zr/Al peaks at the base of the calcareous hardgrounds, where the OPA/UBU boundary was set by Hostettler *et al.* (2017) and Bläsi *et al.* (2013), respectively. In the Weiach succession, the main Zr/Al peak lies at the top of the calcareous unit, where Matter *et al.* (1987) set the OPA/UBU lithostratigraphic boundary. At Riniken, the Zr/Al ratio exhibits an enrichment within the overall Transition Zone, before drastically decreasing within the upper bounding unit. In some sections, such as Mont Terri and Benken, the Ti/Al ratio shows similar patterns along the OPA/UBU transition, although with lower magnitude.

The ferruginous chemofacies dominates within the rust-red coloured lithology of the upper bounding unit at Riniken and Weiach (KL4). It is generally rich in Fe and displays a relative increase in Ca compared to the Opalinus Clay mudstone facies. This observation is supported by the mineralogical composition of KL4, which is dominated by Fe-oxyhydroxides, Fe-silicates and carbonate cements (see Figure 8). The Fe/Al and Ca/Al profiles are anti-correlated, suggesting their respective distribution within distinct mineralogical phases (see Figures 7 and 8). At Riniken, the presence of dolomitic cement is revealed by high Mg/Al;

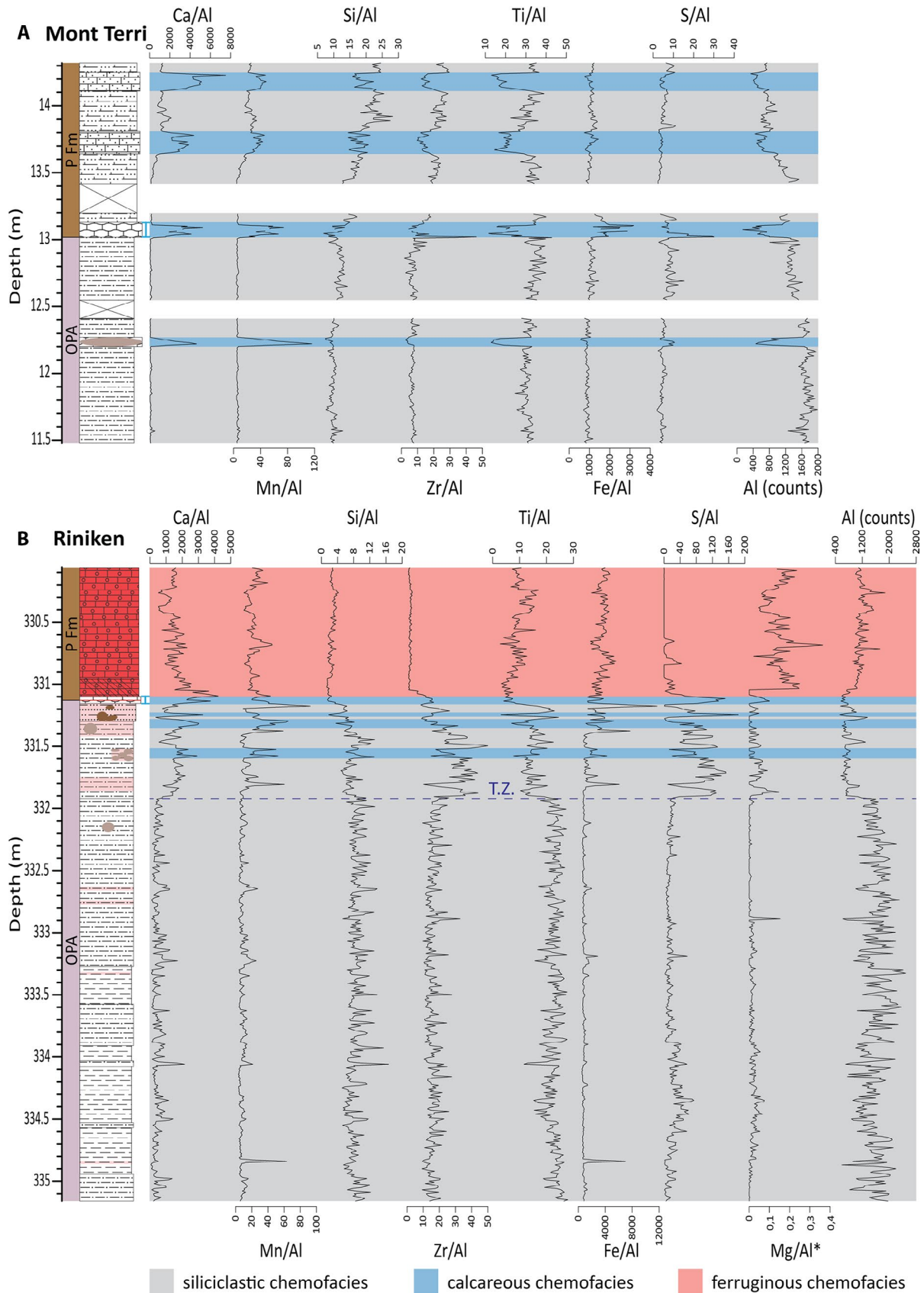


FIGURE 11 Downcore variations of selected element ratios and Al plotted against lithology. Chemofacies are highlighted by different colours. (A) The OPA/UBU transition at Mont Terri. (B) The OPA/UBU transition at Riniken. The OPA/UBU-delineating horizons are highlighted by blue brackets. The beginning of the Transition Zone (T.Z.) is highlighted by the blue dashed line * = Cr-tube; no indication = Mo-tube. OPA = Opalinus Clay; P Fm = Passwang Formation

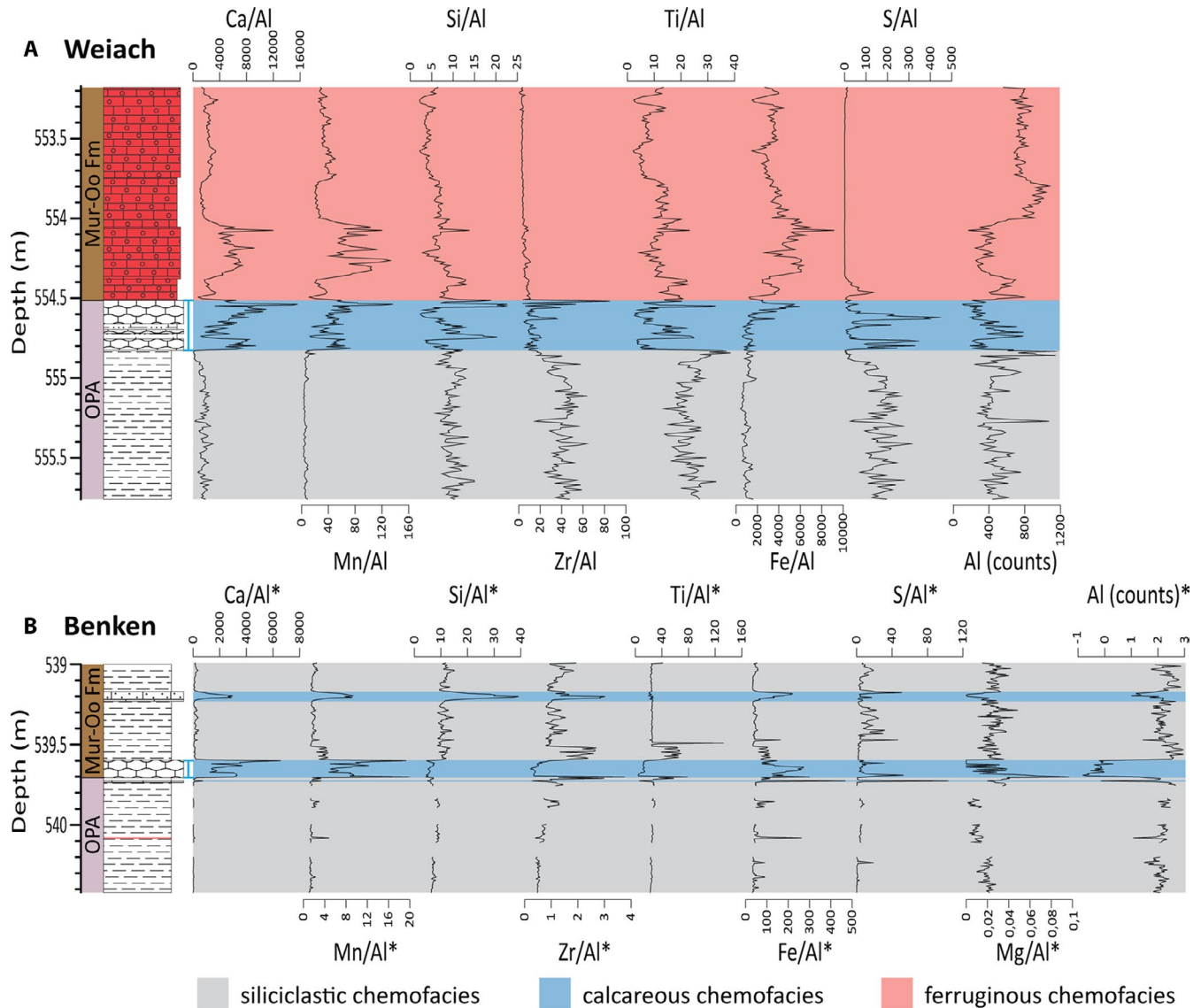


FIGURE 12 Downcore variations of selected element ratios and Al plotted against lithology. Chemofacies are highlighted by different colours. **(A)** The OPA/UBU transition at Weiach. **(B)** The OPA/UBU transition at Benken. The OPA/UBU-delineating horizons are highlighted by blue brackets. * = Cr-tube; no indication = Mo-tube. OPA = Opalinus Clay; Mur-Oo Fm = 'Murchisonae-Oolith Formation'

Mg was only identified in sections screened with the Cr-tube. Within this chemofacies, Al displays a trend similar to Fe, and is comparatively enriched with respect to other elemental proxies for clay minerals (see e.g. the Ti/Al record). The relative Al enrichment combined with the Si decrease (fewer quartz grains, but generally larger) within KL4 is the main reason why the Si/Al ratio cannot be used as a proxy for grain size across the OPA/UBU transition at Riniken and Weiach, but only within similar lithologies. Within the ferruginous chemofacies, Mn/Al correlates positively with Ca/Al, suggesting the preferential incorporation of Mn into carbonate cements, whereas Mn/Al correlates predominantly with Fe/Al within the siliciclastic chemofacies, and thus with the fine siliciclastic fraction. The S content is particularly low within the ferruginous

chemofacies, which agrees with the very rare pyrite within KL4.

To summarise, the XRF-CS data identify different element associations (chemofacies) depending on key lithologies and on their constituent mineralogical fractions. The (a) siliciclastic, (b) calcareous and (c) ferruginous chemofacies can be identified by comparatively high values of (a) terrigenous elements (Si/Al, Ti/Al, Zr/Al, etc.), (b) Ca/Al (and often Mn/Al) and (c) Fe/Al, respectively. The Opalinus Clay mudstone facies and the 'Murchisonae-Oolith Formation' in Benken (KL1) are characterised by the siliciclastic chemofacies, while some heterogeneities display a characteristic calcareous chemofacies (KL3). The Passwang Formation at Mont Terri (KL2) exhibits the mixed-influence of the siliciclastic and the calcareous chemofacies, while the Passwang

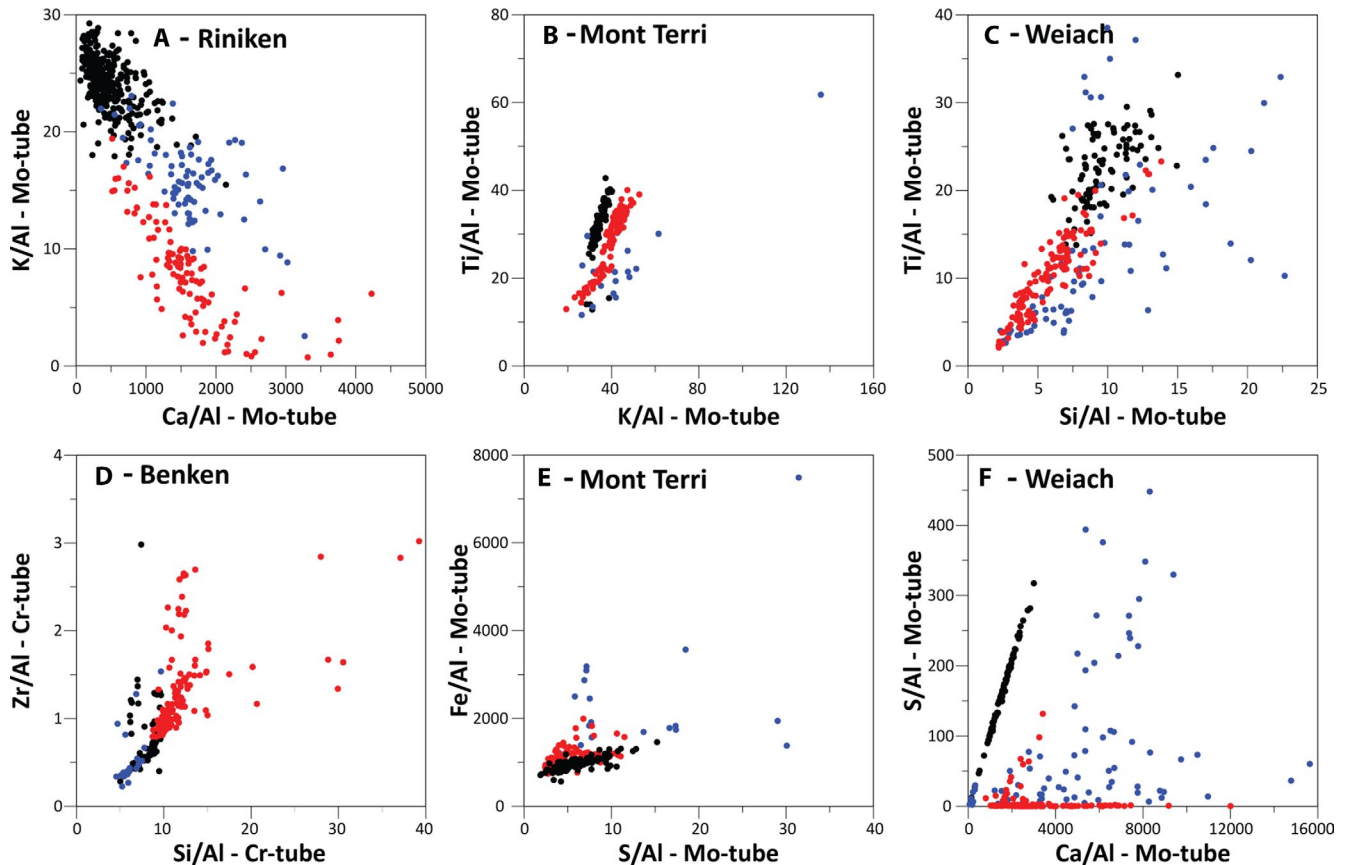


FIGURE 13 Biplots showing correlation trends among selected element ratios. (A) Calcium is anti-correlated towards lithogenic elements. (B) Good correlation among lithogenic elements is illustrated by K and Ti. (C) Good correlation among lithogenic elements is illustrated by Si and Ti. (D) Good correlation among lithogenic elements is illustrated by Si and Zr. (E) Occurrence of pyrite within the Opalinus Clay is evidenced by the good correlation between S and Fe. (F) Occurrence of gypsum at the surface of the Opalinus Clay is evidenced by the good correlation between Ca and S. Colours of data points correspond to lithology: black = Opalinus Clay mudstone facies; blue = OPA/UBU-delineating horizons (Mont Terri, Weiach and Benken) and the whole Transition Zone in the Riniken core; and red = upper bounding unit, respectively, Passwang Formation at Mont Terri and Riniken, and 'Murchisonae-Oolith Formation' at Weiach and Benken

Formation/'Murchisonae-Oolith Formation' at Riniken and Weiach display a ferruginous chemofacies.

The PCA results (Figure 14) illustrate the main correlations among the plotted elements. They show that within siliciclastic-dominated successions, such as those at Mont Terri and Benken, Al, K and Ti correlate strongly together, while Si and Zr differ slightly. This difference is related to their distribution within, respectively, the clay versus the silt/sand fractions, and thus highlights the small grain-size variations (lenticular bedding) exhibited by the downcore elemental profiles. In these successions, Fe is mainly associated with the fine-grained fraction, suggesting a common source. In PCA graphs, Mn plots in-between Ca and Fe (especially at Mont Terri). This feature results from the fact that Mn correlates with Fe within fine-grained, siliciclastic lithologies, while it correlates with Ca within carbonate-rich lithologies. Generally, the Riniken and Weiach successions show similar PCA results. The upper bounding unit (mainly KL4 in these successions) is characterised by high Fe, Mn and Ca, and is negatively correlated with the Opalinus Clay mudstone facies

and its associated detrital element (Al, K, Ti, Si and Zr). Sulphur is poorly correlated with other elements and shows no particular relationship with specific lithological fractions. However, at Mont Terri, S correlates well with Fe, suggesting incorporation into dispersed pyrite framboids. In the other successions, the low positive correlation of S with Ca and Zr points to their co-enrichment within specific intervals, such as hardgrounds (i.e. OPA/UBU-delineating horizons). Overall, the PCA results highlight the differences between the distinct lithologies, and underline the influence of grain-size and mineralogical variations on elemental composition.

5 | DISCUSSION

5.1 | Interpretation of depositional and post-depositional processes

Besides showing great potential for geochemically defining key lithologies along the studied OPA/UBU successions, the

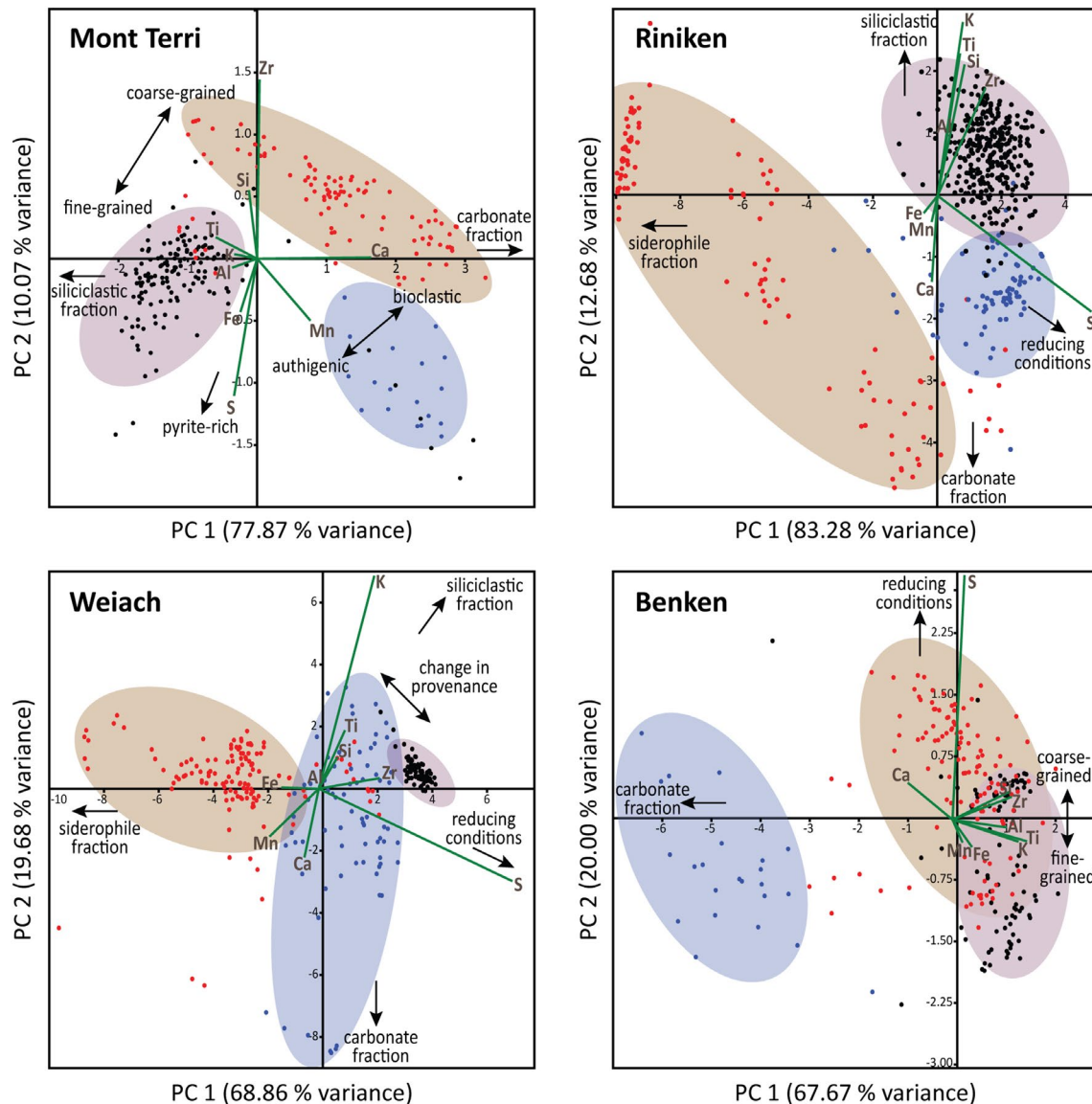


FIGURE 14 Principal component analysis (PCA) of selected elements (Si, Ca, Fe, Al, S, K, Mn and Zr) from each data set. The measured elements were treated using a centred log-ratio transformation. The graph axes differ from one PCA to the other. Colours of data points correspond to lithology: black = Opalinus Clay mudstone facies; blue = OPA/UBU-delineating horizons (Mont Terri, Weiach and Benken) and the whole Transition Zone in the Riniken core; and red = upper bounding unit, respectively, Passwang Formation at Mont Terri and Riniken, and 'Murchisonae-Oolith Formation' at Weiach and Benken. See text for interpretations

downcore element ratios provide information on the depositional and post-depositional processes.

Within this study, the OPA/UBU lithostratigraphic boundary was considered as defined in the current literature (Bläsi *et al.*, 2013; Hostettler *et al.*, 2017; Matter *et al.*, 1987; 1988). However, taking into account the present lithological and geochemical data sets, a slightly different definition of the OPA/UBU boundary can be suggested: that is, the OPA/UBU-delineating horizon could be consistently attributed to either the Opalinus Clay, such as at Riniken and Weiach, or to the upper bounding unit, as at Mont Terri and Benken, allowing for a more homogeneous delineation of these two units.

5.1.1 | The OPA/UBU transition at Mont Terri

From stratigraphic base to top (Figure 11A), the first geochemical heterogeneity (12.21–12.26 m) within the Opalinus Clay mudstone facies consists of a calcareous horizon corresponding to a calcitic nodule, inferred from the congruent Ca/Al and Mn/Al peaks (calcareous chemofacies) and confirmed by petrographic analyses. Such calcitic concretions are frequent within the upper part of the Mont Terri Opalinus Clay and are commonly interpreted as products of early diagenesis (Bläsi *et al.*, 1991; Hostettler *et al.*, 2020; Liniger, 2016). Manganese,

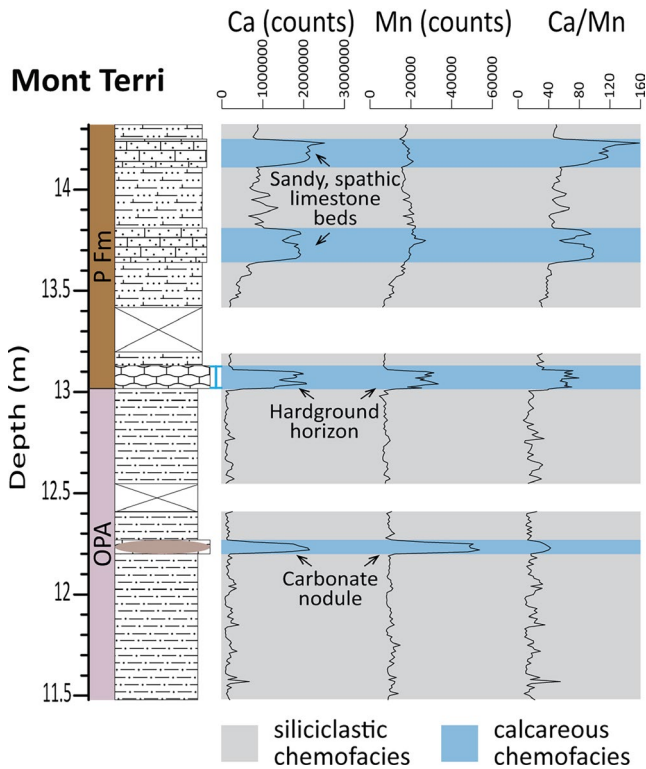


FIGURE 15 Calcium and Mn profiles (in total counts and as ratio) in the Mont Terri core. Type of carbonate beds can be distinguished. The higher the Ca/Mn ratio is the more bioclastic content it shows. Within the Passwang Formation, the positive excursions in the Ca record are not mirrored by the Mn record. The OPA/UBU-delineating horizon is highlighted by the blue bracket. OPA = Opalinus Clay; P Fm = Passwang Formation

within the Opalinus Clay mudstone facies, generally correlates with Fe. These two elements are known to exhibit a similar pattern of redox cycling and to be reduced within the suboxic zone (Froelich *et al.*, 1979; Tribovillard *et al.*, 2006). Yet, in the presence of abundant S and reducing conditions, Fe sulphides form, while Mn either migrates back to the water column, or is incorporated into authigenic carbonates (Tribovillard *et al.*, 2006).

The next Ca/Al and Mn/Al peak along the Mont Terri succession (13.00–13.11 m) reflects the basal intraclastic hardground of the Passwang Formation (OPA/UBU-delineating horizon). The constituent intraclasts are formed mostly by early diagenetic carbonate phases (i.e. micritic/sparitic calcite cement), showing a similar Mn/Al enrichment. In contrast to the previous Ca/Al and Mn/Al heterogeneity, this horizon exhibits a congruent Fe/Al increase, which is attributed to the presence of Fe-ooids, oncolitic ferruginous microbialites and limonitised components. Burkhalter (1995) associated the formation of Fe-ooids and ferruginous microbialites within the Passwang Formation with periods of reduced sedimentation, or non-deposition, related to sea-level changes. He suggested that the OPA/UBU transition comprises a sedimentary discontinuity formed in a water

depth between storm and fair-weather wave base, characterised by the subtle equilibrium between erosion and sedimentation (sediment bypassing). Turbulent conditions and sediment bypassing may also be inferred from the striking Zr/Al peak at the base of the hardground horizon. Hence, erosive currents might have remobilised the lighter sediment fraction (e.g. quartz grains and clay minerals; see also Si/Al to compare) while heavier minerals such as zircon show a relative increase (Craigie, 2018). Petrographic observations within the hardground show an upwards increase in the size of intraclasts, probably related to the increase in hydrodynamic conditions. Eventually, a period of non-deposition at the sediment–water interface started. This bypassing sedimentary discontinuity induced prolonged stable geochemical conditions within the sub sea floor. Intensive sulphate and iron reduction within the sediment probably explain the higher pyrite content (Kasten and Jørgensen, 2000) revealed by the S/Al peak at the base of the hardground. Enhanced production of alkalinity during sulphate reduction also explains simultaneous carbonate precipitation (Curtis, 1977; Wetzel and Allia, 2000). Subsequent lithification of the reworked carbonate components (intraclasts and biolithoclasts) on the sea floor could then occur.

The Si/Al profile reflects a general increase in average grain size, starting at the onset of the Passwang Formation. Silicon is enriched relative to Al, where the amount of quartz grains increases. A congruent increase in calcitic material is inferred from the Ca/Al ratio. Within this interval, Mn follows the Ca trend, caused by the incorporation of Mn within the authigenic calcitic phases cementing the clastic components throughout this lithology. However, the contrasting Ca and Mn signals displayed by the single element profiles within the sandy spathic limestone beds (Figure 15) are associated with a change in composition, and in particular to the relative amount of authigenic versus bioclastic carbonates. Unlike carbonate cements, bioclasts have low Mn concentrations, while both exhibit high Ca intensities (Figure 7). In turn, these two elements may serve to distinguish between primarily short-term accumulations (i.e. bioclastic storm-deposit) and comparatively long-term, diagenetic deposits (i.e. hardgrounds and nodules), enabling process-based correlations.

5.1.2 | The OPA/UBU transition at Riniken

The lenticular bedding within the Opalinus Clay mudstone facies is highlighted by small-scale variations in the Ca/Al and Si/Al ratios (Figure 11B). A more important lithological change is identified by a fairly distinct chemofacies within the Transition Zone (331.90–331.14 m). The XRF-CS data point to a relative increase in carbonate (Ca/Al), Fe sulphides (S/Al) and heavy minerals (Zr/Al) within this zone. The Fe/Al and Mn/Al ratios display several peaks that can be linked to

the occurrence of sideritic nodules, and/or horizons of Fe-oxidation during core storage (mainly from siderite or pyrite). The combination of these proxies and petrographic observations point to a period with slower sedimentation rates, marking perhaps the onset of a regression, as postulated by Burkhalter (1995; 1996). An increase in transport energy can be inferred from the relative enrichment in bioclastic debris and heavy minerals, while the presence of several diagenetic concretions and a higher pyrite content are both hints for longer residence time within stable geochemical conditions, typically within the sulphate reduction zone (Wetzel and Allia, 2000).

The erosive discontinuity (331.34 m) within the Transition Zone marks the beginning of a condensed, sideritic interval, which comprises sedimentary signs of intensive erosion and reworking (intraclasts, reworked nodules and coarse bioclasts). Siderite precipitation requires reducing conditions, high concentrations of reactive Fe, high alkalinity and negligible sulphide in pore waters (Berner, 1981; Taylor and Macquaker, 2011). Lerouge *et al.* (2014) suggested that sideritic concretions within the Opalinus Clay formed close to the sediment/water interface, at a fluctuating boundary between the suboxic and sulphate reduction zones, and that disseminated siderite precipitated during bacterial methanogenesis and associated production of alkalinity following consumption of HS⁻ by Fe sulphide precipitation. Within this condensed interval pyrite is scarce to absent (excluding intraclasts), an observation supported by the low S/Al. The sideritization event might therefore have occurred before reaching the sulphate reduction zone. Aller *et al.* (1986), for example, demonstrated that within environments with abundant Fe, siderite might have already precipitated during suboxic diagenesis (also referred to as non-sulphidic-post-oxic sensu Berner, 1981). In fact, the abundance of Fe-oxides might inhibit or postpone sulphate reduction (Chapelle and Lovley, 1992; Lovley and Phillips, 1987), and hence provide prolonged suboxic, non-sulphidic conditions for siderite precipitation. Taylor and Curtis (1995) suggested a similar process for the formation of sideritic ironstone from the Lower Jurassic of England. However, within the scope of this study, it is not possible to exclude the precipitation of siderite during methanogenesis.

The sideritic condensed interval is topped by thin, successive, calcareous, Fe-oidal beds (high Ca/Al; layers a to d in Figure 7), which are considered by Matter *et al.* (1987) to be the lithostratigraphic top of the Opalinus Clay. The individual layers, which display small differences in composition, were most probably formed as successive events of symsedimentary lithification of bioclastic debris on the sea floor, associated with sediment starvation (indicated by the presence of drusy, isopachous and microsparitic/micritic cements; Wilson and Palmer, 1992). They mark the top of the Transition Zone and its associated chemofacies, and hence, of the postulated sedimentary discontinuity (Burkhalter, 1995). Layer d shows abundant well-rounded Fe-oids and coarse bioclastic fragments, which may indicate

sediment bypassing under turbulent conditions. Prolonged stable geochemical conditions can be inferred by the high degree of pyritization of the ooids present within the top layer.

The onset of the Passwang Formation is marked by a change in sedimentation regime and sediment type. The Fe-rich lithology points to a markedly different depositional environment, possibly related to increased input of weathered lateritic soil (see also Burkhalter, 1995). This conclusion is confirmed by the enrichment of low-solubility and mostly incompatible elements Fe and Al, relative to other detrital elements typically present within the Opalinus Clay (Si, Ti, K, etc.). The Si/Al ratio, in particular, shows an unambiguous decrease at the onset of the Passwang Formation that supports a lateritic origin. Deeply weathered lateritic soil profiles are commonly characterised by intense chemical depletion of soluble elements such as Si and K, and residual enrichment of less soluble elements such as Fe and Al often in the form of Fe and Al-oxyhydroxides and clay minerals (typically kaolinite; Tardy and Nahon, 1985). The drastic Mg increase within the Fe-rich lithology is mostly related to the occurrence of dolomite (ankerite) cement.

The basal Passwang Formation is classically interpreted as a depositional environment characterised by predominantly oxic conditions, notably due to the presence of abundant goethite/limonite and to a high level of bioturbation (Bläsi, 1987; Burkhalter, 1995; 1996; Matter *et al.*, 1987). Its lowermost cross-bedded unit (uppermost part of the slab on Figure 7) suggests deposition within energetic bottom-water currents. Sediment deposition may occur as sand-wave complexes, such as those interpreted for the Minette ironstone from Luxembourg and Lorraine (Teyssen, 1984). The Minette ironstone shows a similar enrichment in Fe and Al, as well as Cr and V (also observed within this study; Siehl and Thein, 1989). The highly bioturbated lithology of the upper part obscures any sedimentary structures, and might also be responsible for the limited organic matter and the very low pyrite content, such as highlighted by the low S/Al ratio.

5.1.3 | The OPA/UBU transition at Weiach

Core observations and the tight correlation between Ca/Al and S/Al in Figure 13 suggests that the Opalinus Clay has been strongly affected by alteration during core storage. The precipitation of gypsum, as an alteration product, is common on Opalinus Clay cores acquired a long time ago, tunnel faces and outcrops (Mäder and Mazurek, 1998). It reflects the oxidative breakdown of pyrite (or siderite) and dissolution of calcite (and dolomite) by sulphuric acids (Mäder and Mazurek, 1998). It typically forms in small fractures induced by unloading and partial transient desaturation.

At Weiach (Figure 12A), in contrast to Mont Terri or Benken, the OPA/UBU-delineating horizon (554.82–554.50 m) is stratigraphically attributed to the Opalinus Clay (Bläsi, 1987; Bläsi *et al.*, 2013; Matter *et al.*, 1988). However, from a geochemical perspective, it shares similarities with the OPA/UBU-delineating horizons at Mont Terri and at Benken expressed by the significant increase in Ca, Mn, and partly S and Fe. The Weiach interval is nonetheless three times thicker. Two main carbonate beds are separated by a more siliciclastic interval expressing a fining-upwards sequence, as suggested by the Si/Al and Ti/Al ratios. This overall interval can be related to two successive periods of sediment starvation and in-situ lithification of the sea floor (see also two main S/Al peaks indicating periods of stable geochemical conditions within the carbonate beds). The position of the highest Zr/Al peak suggests that the main episode of prolonged sediment bypassing lies at the top of the calcareous interval, where Bläsi (1987) and Matter *et al.* (1988) set the OPA/UBU lithostratigraphic boundary. These authors postulated that the calcareous unit marks the top horizon of an overall coarsening-upwards sequence, or a so-called 'Dachbank' cycle (see also Wetzel and Allia, 2003), formed by hardening (and reworking) of the top Opalinus Clay sediment. Increasing hydrodynamics and associated reduced sedimentation rates within this interval can be supported by increasing trends of, respectively, Zr/Al (heavy minerals accumulation) and Fe/Al. Iron enrichment, for instance as pyrite, may point to suboxic and/or anoxic conditions within the sub sea floor. Part of the Fe increase may nonetheless be attributed to the higher content of Fe-ooids within this interval.

The lithology and chemofacies of the basal 'Murchisonae-Oolith Formation' exhibit strong similarities with the basal portion of the Passwang Formation at Riniken. A similar mature sediment, composed mainly of the erosive product of continental laterite weathering profiles, can be postulated (Tardy and Nahon, 1985). High-energy bottom-water currents at the base of this unit are, however, not always highlighted (absence of cross-bedding), in contrast to the sequence at Riniken. This sediment type (KL4) differs from its lithostratigraphic equivalents in Mont Terri and Benken, which could be explained by differences in sediment source and/or related to sub-basin topography. The small regional extent of KL4 at the base of the upper bounding unit could point to a single, regional Fe-ooidal sedimentary complex covering the area of Riniken and Weiach, resembling the sand-wave structures interpreted further north, within the South German Basin (Bayer and McGhee, 1985) and in Luxembourg and Lorraine (Teyssen, 1984).

5.1.4 | The OPA/UBU transition at Benken

The succession at Benken (Figure 12B) mostly resembles the Mont Terri transition. Few S/Al, Fe/Al and Mn/Al peaks

points to very limited heterogeneities within the Opalinus Clay mudstone facies. They correspond to pyritic and altered sideritic horizons. The uppermost S/Al peak within the Opalinus Clay highlights pyritised burrow traces occurring below the OPA/UBU-delineating horizon (539.70–539.60 m) of the 'Murchisonae-Oolith Formation'. Pyritization might have occurred through early diagenetic replacement of the organic matrix left by the burrower (Schieber, 2002). Abundant infaunal benthos is also consistent with a prolonged sedimentation break at the top of the Opalinus Clay, and the establishment of a benthic hardground community (Wilson and Palmer, 1992). As for Mont Terri, the main heavy minerals enrichment peak (Zr/Al, Ti/Al; Ti being also strongly associated with ilmenite and rutile; Craigie, 2018) occurs at the base of the hardground (OPA/UBU-delineating horizon). The latter shares strong geochemical similarities with the Mont Terri hardground, which all point to similar formation conditions, that is, lithification of reworked intraclastic material during a period of prolonged stable geochemical conditions related to increased hydrodynamics.

Visually, the overlying basal 'Murchisonae-Oolith Formation' differs little from the Opalinus Clay mudstone facies, which was the main reason they were formerly included within same lithostratigraphic unit (Bläsi *et al.*, 2013; Nagra, 2001). The chemofacies, however, reveals slightly coarser material (Si/Al, Zr/Al) within the 'Murchisonae-Oolith Formation' and a higher pyrite content (S/Al). The PCA (Figure 14) provides a further argument for identifying two distinct lithologies, although less differentiated than the equivalent formations within the other core sections. The Ti/Al and Zr/Al ratios display a strong enrichment a few centimetres above the hardground, which is consistent with higher transport energy and sediment bypassing through the OPA/UBU transition.

5.1.5 | Genesis of the OPA/UBU transition

While each location has its particularities, a major change in sediment composition and associated chemofacies can be observed at all studied locations throughout the OPA/UBU transition. The trend towards more carbonate-rich lithologies is also known from the literature (Bläsi, 1987; Burkhalter, 1996; Burkhalter *et al.*, 1997; Hostettler *et al.*, 2017; 2020; Wetzel and Allia, 2003). The relative increase in grain-size and bioclastic content points to a depositional environment influenced by shallower water depths and/or an increase in current strength. Sediment bypassing suggested by petrographic and geochemical proxies indicates a period of enhanced hydrodynamic activity during the OPA/UBU transition. The sudden lateritic signature of the upper bounding unit at Riniken and Weiach highlights a significant change in sediment source and type, which probably resulted

from combined hydrodynamic and palaeoclimate factors (Burkhalter, 1995; Teyssen, 1989). The change in sediment provenance and related hydrodynamic conditions was proposed by Burkhalter (1996), who suggested based on quartz grain-size analysis that terrestrial sediment delivery changed from a (north)west–(south)east direction during the deposition of the Opalinus Clay, to a north(west)–south(east) direction during the deposition of the basal Passwang Formation. While relationships between sediment type, provenance and distribution, and their link with hydrodynamic settings and palaeoclimate are difficult to assess within the scope of this work, it appears that the OPA/UBU boundary falls within a period of major tectonic, hydrodynamic and palaeoclimate perturbations across the epicontinental Central European Basin (Mid-Cimmerian events; de Graciansky and Jacquin, 2003; Underhill and Partington, 1993). The early Aalenian was tectonically active, notably due to the opening of the Atlantic and Tethys oceans (Lemoine *et al.*, 1986; Ziegler, 1988), which had a major effect on the sea floor topography, as well as on sediment deposition (Durllet *et al.*, 1997; Teyssen, 1989; Wetzel *et al.*, 2003). Moreover, a major doming event uplifted the area around the North Sea (Underhill and Partington, 1993), which subsequently modified the overall circulation patterns across the epicontinental Central European Basin. In turn, a generally cooler period was initiated, due in particular to the obstruction of a northward flowing current through the Viking Corridor and consequently reduced heat transfer from the Tethys towards the Boreal Ocean (Korte *et al.*, 2015; Price, 2010).

5.2 | XRF-CS for unravelling the formation of sedimentary discontinuities: example of the OPA/UBU transition

The use of XRF-CS as a tool for delineating stratigraphic sequences within Mesozoic rock formations is relatively novel. For instance, Thöle *et al.* (2020) applied the method to drill cores covering the Berriasian to Aptian interval within the Lower Saxony Basin (northern Germany). They identified several elemental ratio proxies allowing them to correlate proximal and distal basinal environments, and to characterise the studied successions in terms of grain-size and carbonate content variations using Si/Al and Ca/Ti, respectively. The authors used continuous XRF-CS records to identify transgressive and regressive systems tracts, being a suitable tool for establishing sequence stratigraphic frameworks. The present study differs from the work of Thöle *et al.* (2020), as it focusses on a limited stratigraphic interval, and on the detailed characterisation of one particular sequence boundary (i.e. discontinuity surface). It shows nonetheless that similar proxies can be used to trace variations in grain-size and carbonate content (Si/Al, Zr/Al and Ca/Al). It reveals moreover

that element ratios have the potential to detect sedimentary discontinuities and to identify their formation processes, such as illustrated by the combination of Zr/Al, Ti/Al, S/Al, Ca/Al and Mn/Al ratios within the four case studies.

The hypothesis of using geochemical proxies for determining differential accumulation of heavy minerals to trace sedimentary discontinuities (particularly Zr/Al peaks) is supported by petrographic arguments, notably the congruent presence of hardgrounds and typically high-energy deposits (i.e. intraclasts, Fe-oids) that are classically linked to erosive processes or sediment bypassing within similar successions (Burkhalter, 1995; Teyssen, 1989; Wetzel and Allia, 2000), and the presence of petrographic and geochemical arguments inferring prolonged, stable geochemical conditions within the sub sea floor. The method can hence be used to differentiate among different types of sedimentary discontinuities. Burkhalter (1995) differentiated three types of discontinuity surfaces (comparable to third-order sequence boundaries; Van Wagoner *et al.*, 1988): (a) regressional discontinuities, (b) transgressional discontinuities and (c) omissional discontinuities. Regressional discontinuities separate low-energy highstand deposits from lowstand deposits during regressive phases. They are formed by sediment bypassing or erosion, when the rate of sea-level fall equals or exceeds the rate of sea-floor subsidence. Transgressional discontinuities separate high-energy lowstand deposits from transgressional deposits. They are generated by non-deposition caused by sediment bypassing at the onset of sea-level rise. Omissional discontinuities correspond to maximum flooding surfaces and are formed by sediment starvation.

The geochemical characterisation of the OPA/UBU transition suggests a period of sediment non-deposition due to sediment bypassing during an overall regressive trend, as supported by the lithofacies assemblages and associated chemofacies (i.e. increase in coarser terrigenous and bioclastic content). The results are thus generally in accordance with Burkhalter (1995; 1996) and Burkhalter *et al.* (1997), who interpreted the OPA/UBU boundary as a widespread regressional discontinuity during the early Aalenian. The authors suggested that this boundary marks the top of the low-energy highstand deposit (the Opalinus Clay mudstone facies; KL1), at the onset of a relative sea-level fall, when water energy was at its maximum and prevented sediment deposition (i.e. sediment bypassing), before the overlying lowstand deposit (the upper bounding unit) started to accumulate. The limited vertical extent of the investigated intervals, however, does not allow for confirmation, or rejection, of the interpretation that the OPA/UBU transition reflects a single event throughout northern Switzerland (Burkhalter, 1996) rather than more localised processes related to the palaeogeographic and topographic setting. Similar geochemical signals can be expected within any intra-formational hiatus formed by comparable bypassing processes (but probably of lower intensity).

An overall regressive trend during the early Aalenian is nonetheless suggested from other locations across the epicontinental Central European Basin (Callomon, 2003; de Graciansky and Jacquin, 2003; Sandoval *et al.*, 2002; Teyssen, 1989; Zimmermann *et al.*, 2015; 2018), supporting the interpretation of Burkhalter (1996). Zimmermann *et al.* (2015) proposed a comprehensive framework of second-order, third-order and fourth-order Lower and Middle Jurassic sequences in the North German Basin. They evidenced the occurrence of one third-order sequence (Aa1) and two fourth-order sequences (Aa1a and Aa1b) of predominantly Aalenian age. The third-order sequence started during the Levesquei Zone (beginning of the transgressive phase) and lasted up to the Bradfordensis Zone (end of the regressive phase), with the maximum flooding which lasted about 4.3 Myr taking place within the early Aalenian (Opalinus Zone) Opalinuston shales (i.e. Opalinuston Formation *sensu* Franz and Nitsch, 2009). It is suggested that the fourth-order sequence (Aa1a) began simultaneously with the onset of the third-order sequence, but terminated within the early Murchisonae Zone, reflecting the maximum flooding within the Opalinuston Formation. Closer to the study area, northwards and westwards from Mont Terri (i.e. Burgundy and Alsace, France), the upper Toarcian and overall Aalenian successions are thin to strongly condensed, or absent in certain locations representing possibly emerged areas (Contini, 1970; Durllet and Thierry, 2000; de Graciansky and Jacquin, 2003; Schirardin, 1960). The scarcity and absence of late Toarcian and Aalenian deposits are interpreted as the result of an overall regressive trend, reflecting the shallow, high-energy water conditions and the associated sediment non-deposition, on an area that used to be a topographic high bordering the Paris Basin, the Burgundy High (de Graciansky and Jacquin, 2003; Durllet and Thierry, 2000).

Considering the above-mentioned context of a major regressive trend across the epicontinental Central European Basin during the early Aalenian, the OPA/UBU transition can be interpreted as a fourth-order regressive phase, superimposed by an overall third-order regressive half-cycle, where the OPA/UBU boundary reflects the regression discontinuity of the earliest Aalenian, fourth-order, sea-level fall (Aa1a *sensu* Zimmermann *et al.*, 2015). The overall deposition of the Opalinus Clay and its upper bounding unit is however more complicated, as it was strongly influenced by differential subsidence (Burkhalter, 1996; Burkhalter *et al.*, 1997; Wetzel *et al.*, 2003; Wetzel and Allia, 2000; 2003; Wetzel and Meyer, 2006). Deeper depocenters (topographic lows) formed when the subsidence rate exceeded the eustatic sea-level fall, creating different sub-basins within the depositional area. These depocenters were situated below the storm-wave base, enabling the accumulation of comparatively more parasequences than the neighbouring topographic highs. On the

other hand, the highs were situated above the storm-wave base and affected by storm-induced, erosive currents that were responsible for the establishment of sedimentary discontinuities (Burkhalter *et al.*, 1997; Wetzel and Allia, 2000; 2003). Depending on location, it resulted in the accumulation of varying numbers of successive high-order parasequences (Bläsi, 1987; Bläsi *et al.*, 2013; Burkhalter, 1996; Burkhalter *et al.*, 1997). It might also explain parts of the diachronous, biostratigraphic framework of the OPA/UBU transition (Bläsi *et al.*, 2013; Hostettler *et al.*, 2020; Wohlwend *et al.*, 2019). Hence, the Mont Terri Opalinus Clay succession exhibits two major coarsening-upwards sequences that can be interpreted as two fifth-order parasequences during the Opalinus Subzone (Lauper *et al.*, 2018). Further to the east, the Opalinus Clay is characterised by one overall shallowing-upwards sequence (third order and fourth order), with higher order, 'Dachbank' cycles occurring within the upper part of the succession, and so, probably younger subsidence pulses provided the new accommodation space (Bläsi, 1987; Burkhalter *et al.*, 1997; Wetzel and Allia, 2003). It has been shown from other locations across the epicontinental Central European Basin that differential subsidence played a major role in the formation of high-order parasequences which imprinted the overall eustatic cyclicity (Durllet *et al.*, 1997; de Graciansky and Jacquin, 2003; Teyssen, 1989). It thus supports the interpretation provided for the Swiss northern basin (Bläsi, 1987; Burkhalter, 1995; 1996; Burkhalter *et al.*, 1997; Wetzel and Allia, 2000; 2003).

Based on petrographic criteria alone, especially when investigating subsurface successions that are limited to the study of drill cores, it may be difficult to assess the genetic origin of sedimentary discontinuities (given that they can be identified as such), as well as to understand their significance in terms of sequence stratigraphy. It has already been shown that the use of elemental proxies can be convenient for identifying and characterising stratigraphic sequences within mudstone-dominated successions (Thöle *et al.*, 2020; Turner *et al.*, 2016; Ver Straeten *et al.*, 2011). The present study nonetheless highlights the potential of XRF-CS as an additional and complementary tool for unravelling the depositional history of complex and mixed, carbonate-siliciclastic transitions. Discontinuity surfaces and sequence boundaries may be delineated and recognised among different discontinuity types and formation processes, and related to their sequence stratigraphic context. Furthermore, as several geochemical proxies are largely process-based, and in this case can be related to major events (i.e. a major sea-level fall and a longer period of sediment non-deposition), they may enable chemostratigraphic correlations within areas controlled by specific sedimentation regimes, even though they might be overprinted by differential subsidence and associated basin subdivision, and reflect distinct biostratigraphic constraints.

6 | CONCLUSIONS

The study of the OPA/UBU lithostratigraphic transition suggests that XRF-CS is successful in identifying, characterising and delineating major lithological units and boundaries in a time-effective, continuous and non-destructive way. It provides additional objective and quantitative support to petrographic and lithostratigraphic studies. Furthermore, XRF-CS elemental proxies allow tracking of subtle grain-size and mineralogical variations that are difficult to identify by visual observations only. They help in deciphering complex depositional environments, allowing a better comprehensive understanding of depositional and diagenetic processes, the last being crucial for correlation studies in complex basins.

The combined use of detailed petrography and XRF chemostratigraphy in this study (a) provides evidence of the change in sediment type and sedimentation regime across the OPA/UBU lithostratigraphic transition, (b) identifies sediment bypassing as the major process responsible for the OPA/UBU sedimentary discontinuity and (c) disentangles the main depositional and diagenetic processes along the overall transition.

The combined use of sedimentary petrography and XRF chemostratigraphy, the latter providing high-resolution elemental variations and element peak-markers, is important for establishing process-based correlations at basin scale, within lithologically heterogeneous and biostratigraphically diachronous sedimentary successions.

ACKNOWLEDGEMENTS

The following people are warmly acknowledged for their precious time and contribution: Marina Morlock (Bern) for her help with XRF core scanning; Melissa Morel and Christoph Neururer (Fribourg) for their help with SEM-EDX analyses; Valentin Rime (Fribourg) for helping with a figure; Géraldine Zimmerli, Anja Amrein, Andrea Buckley (OPA-team), as well as Patrick Dietsche, Alexandre Salzmann (Fribourg), Felix Stefani (Nagra) and the Mont Terri team, for their technical and logistical support with drill core, sample and thin section handling and preparation. Daniel Traber (Nagra), Peter Swart (journal editor) and two anonymous reviewers are thanked for their helpful comments on (an earlier version of) the manuscript. This work is part of a PhD project co-funded by the Swiss National Cooperative for the Disposal of Radioactive Waste (Nagra) and the Swiss Federal Office of Topography swisstopo. Part of the funding is provided through the SO-C experiment of the Mont Terri Project. These generous contributions are highly appreciated.

CONFLICT OF INTEREST

The authors declare no conflict of interest.

DATA AVAILABILITY STATEMENT

The data that support the findings of this study are available from the corresponding author upon reasonable request.

ORCID

Bruno Lauper  <https://orcid.org/0000-0002-0760-243X>

Hendrik Vogel  <https://orcid.org/0000-0002-9902-8120>

Daniel Ariztegui  <https://orcid.org/0000-0001-7775-5127>

Anneleen Foubert  <https://orcid.org/0000-0002-9011-9683>

REFERENCES

- Aitchison, J. (1986) *The Statistical Analysis of Compositional Data*. London: Chapman & Hall.
- Aller, R.C., Mackin, J.E. and Cox, R.T. Jr (1986) Diagenesis of Fe and S in Amazon inner shelf muds: apparent dominance of Fe reduction and implication for genesis of ironstones. *Continental Shelf Research*, 24, 2455–2486.
- Bayer, U. and McGhee, G.R. (1985) Evolution in marginal epicontinental basins: the role of phylogenetic and ecological factors. In: Bayer, U. and Seilacher, A. (Eds.) *Sedimentary and Evolutionary Cycles*. Berlin: Springer, pp. 164–220.
- Berner, R.A. (1981) A new geochemical classification of sedimentary environments. *Journal of Sedimentary Petrology*, 51(2), 359–365.
- Bläsi, H.-R. (1987) Lithostratigraphie und Korrelation der Doggersedimente in den Bohrungen Weiach, Riniken und Schafisheim. *Eclogae Geologicae Helveticae*, 80, 415–430.
- Bläsi, H.-R., Deplazes, G., Schellmann, M. and Traber, D. (2013) Sedimentologie und Stratigraphie des ‘Braunen Doggers’ und seiner westlichen Äquivalente. Nagra Arbeitsbericht, NAB 12–51, Nagra, Wettingen, Switzerland.
- Bläsi, H.-R., Peters, T. and Mazurek, M. (1991) Der Opalinus-Ton des Mt. Terri (Kanton Jura): Lithologie, Mineralogie und physiko-chemische Gesteinsparameter. Nagra Interner Bericht. Nagra, Wettingen, Switzerland.
- Bloemsma, M.R., Zabel, M., Stuut, J.B.W., Tjallingii, R., Collins, J.A. and Weltje, G.J. (2012) Modelling the joint variability of grain size and chemical composition in sediments. *Sedimentary Geology*, 280, 135–148.
- Bossart, P., Bernier, F., Birkholzer, J., Bruggeman, C., Connolly, P., Dewonck, S. et al. (2017) Mont Terri rock laboratory, 20 years of research: introduction, site characteristics and overview of experiments. *Swiss Journal of Geosciences*, 110, 3–22.
- Bossart, P. and Thury, M. (2008) Mont Terri Rock Laboratory. Project, programme 1996 to 2007 and results. Reports of the Swiss Geological Survey, No. 3. Federal Office of Topography (swisstopo), Wabern, Switzerland.
- Burkhalter, R.M. (1995) Ooidal ironstones and ferruginous microbials: origin and relation to sequence stratigraphy (Aalenian and Bajocian, Swiss Jura mountains). *Sedimentology*, 42, 57–74.
- Burkhalter, R.M. (1996) Die Passwang-Alloformation (unteres Aalénien bis unteres Bajocien) im zentralen und nördlichen Schweizer Jura. *Eclogae Geologicae Helveticae*, 89, 875–934.
- Burkhalter, R.M., Bläsi, H.-R. and Feist-Burkhardt, S. (1997) Der «Dogger» (oberes Aalénien) in den Bohrungen Herdern-1, Berlingen-1 und Kreuzlingen-1 (Nordostschweiz) und seine Beziehung zu den gleichaltrigen Schichten im Nordjura. *Eclogae Geologicae Helveticae*, 90, 269–291.

- Burkhalter, R.M. and Heckendorn, W. (2009) Das Stratigraphische Komitee der Schweiz (SKS). *Swiss Bulletin für angewandte Geologie*, 14(1+2), 159–162.
- Callomon, J.H. (2003) The Middle Jurassic of western and northern Europe: its subdivisions, geochronology and correlations. *Geological Survey of Denmark and Greenland Bulletin*, 1, 61–73.
- Calvert, S.E. and Pedersen, T.F. (2007) Chapter fourteen elemental proxies for palaeoclimatic and palaeoceanographic variability in marine sediments: interpretation and application. *Developments in Marine Geology*, 1, 657–644.
- Chapelle, F.H. and Lovley, D.R. (1992) Competitive exclusion of sulfate reduction by Fe(III)-reducing bacteria: a mechanism for producing discrete zones of high-iron ground water. *Ground Water*, 30(1), 29–36.
- Chatellier, J.-Y., Simpson, K., Perez, R. and Tribouvillard, N. (2018) Geochemically focused integrated approach to reveal reservoir characteristics linked to better Montney productivity potential. *Bulletin of Canadian Petroleum Geology*, 66(2), 516–551.
- Contini, D. (1970) L'Aalénien et le Bajocien du Jura Franc-Comtois. PhD thesis, University of Besançon, Besançon, France.
- Craigie, N. (2018) *Principles of Elemental Chemostratigraphy. A Practical User Guide*. Cham: Springer International Publishing AG.
- Croudace, I.W., Rindby, A. and Rothwell, R.G. (2006) ITRAX: description and evaluation of a new multi-function X-ray core scanner. *Geological Society, London, Special Publications*, 267(1), 51–63.
- Croudace, I.W. and Rothwell, R.G. (Eds) (2015) *Micro-XRF Studies of Sediment Cores: Applications of a Non-destructive Tool for the Environmental Sciences*. Dordrecht: Springer Science+Business Media B. V.
- Curtis, C.D. (1977) Sedimentary geochemistry: environments and processes dominated by involvement of an aqueous phase. *Philosophical Transactions of the Royal Society of London. Series A, Mathematical and Physical Sciences*, 286(1336), 353–372.
- Cuven, S., Francus, P. and Lamoureux, S.F. (2010) Estimation of grain size variability with micro X-ray fluorescence in laminated lacustrine sediments, Cape Bounty, Canadian High Arctic. *Journal of Paleolimnology*, 44(3), 803–817.
- de Graciansky, P.-C. and Jacquin, T. (2003) Evolution des structures et de la paléogéographie au passage Lias-Dogger dans le bassin de Paris d'après les données de la subsurface. *Bulletin de la Société Géologique de France*, 174(1), 3–17.
- Deplazes, G., Meckler, A.N., Peterson, L.C., Hamann, Y., Aeschlimann, B., Günther, D. et al. (2019) Fingerprint of tropical climate variability and sea level in sediments of the Cariaco Basin during the last glacial period. *Sedimentology*, 66(5), 1967–1988.
- Dickson, J.A.D. (1965) A modified staining technique for carbonates in thin section. *Nature*, 205, 587.
- Dunham, R.J. (1962) Classification of carbonate rocks according to depositional texture. In: Ham, W.E. (Ed.) *Classification of Carbonate Rocks. Memoir of the American Association of Petroleum Geologists*, 1, 108–121.
- Durlet, C., Jacquin, T. and Floquet, M. (1997) Tectonique syn-sédimentaire distensive dans les calcaires aaléno-bajociens du Seuil de Bourgogne (France). *Comptes Rendus de l'Académie des Sciences-Series IIA-Earth and Planetary Science*, 324(12), 1001–1008.
- Durlet, C. and Thierry, J. (2000) Modalités séquentielles de la transgression aaléno-bajocienne sur le sud-est du Bassin parisien. *Bulletin de la Société Géologique de France*, 171(3), 327–339.
- Etter, W. (1990) Paläontologische Untersuchungen im unteren Opalinuston der Nordschweiz. PhD thesis, University of Zurich, Zurich, Switzerland.
- Feist-Burkhardt, S. (2012) Palynostratigraphie des Mittleren Jura. Nagra Arbeitsbericht, NAB 12-57, Nagra, Wettingen, Switzerland.
- Franz, M. and Nitsch, E. (2009) Zur lithostratigraphischen Gliederung des Aalenium in Baden-Württemberg. *LGRB Informationen*, 22, 123–146.
- Froelich, P.N., Klinkhammer, G.P., Bender, M.L., Luedtke, N.A., Heath, G.R., Cullen, D. et al. (1979) Early oxidation of organic matter in pelagic sediments of the eastern equatorial Atlantic: suboxic diagenesis. *Geochimica et Cosmochimica Acta*, 43, 1075–1090.
- Gygax, E., Schefer, S. and Jaeggi, D. (2017) PE Experiment: Drillcore documentation of prospecting boreholes BPE-1, BPE-2 and BPE-3, including an adapted geological map of the Mont Terri rock laboratory. Mont Terri Technical Note, TN 2017–52. Federal Office of Topography (swisstopo), Wabern, Switzerland.
- Hammer, Ø., Harper, D.A. and Ryan, P.D. (2001) PAST: paleontological statistics software package for education and data analysis. *Palaeontologia Electronica*, 4(1), 9.
- Hostettler, B., Dietze, V., Jaeggi, D. and Menkveld-Gfeller, U. (2020) Ammonite stratigraphy and fossils of the Passwang Formation (Middle Jurassic) and the Opalinus Clay (Lower to Middle Jurassic) excavated in Ga 18 and the Niches 1, 5 and 8 in the Mont Terri Rock Laboratory. Mont Terri Technical Report, TR 2018–01, Federal Office of Topography (swisstopo), Wabern, Switzerland.
- Hostettler, B., Reisdorf, A.G., Jaeggi, D., Deplazes, G., Bläsi, H.-R., Morard, A. et al. (2017) Litho- and biostratigraphy of the Opalinus Clay and bounding formations in the Mont Terri rock laboratory (Switzerland). *Swiss Journal of Geosciences*, 110, 22–37.
- Irving, E. (1977) Drift of the major continental blocks since the Devonian. *Nature*, 270, 304–309.
- Jaccard, S.L., Haug, G.H., Sigman, D.M., Pedersen, T.F., Thierstein, H.R. and Röhl, U. (2005) Glacial/interglacial changes in subarctic North Pacific stratification. *Science*, 308, 1003–1006.
- Kaboth-Bahr, S., Denis, V., Su, C.-C., O'Regan, M., Gyllencreutz, R., Jakobsson, M. et al. (2019) Deciphering ~45,000 years of Arctic Ocean lithostratigraphic variability through multivariate statistical analysis. *Quaternary International*, 514, 141–151.
- Kasten, S. and Jørgensen, B.B. (2000) Sulfate reduction in marine sediments. In: Schulz, H.D. and Zabel, M. (Eds.) *Marine Geochemistry*. Berlin, Heidelberg: Springer, pp. 263–281.
- Kneuker, T., Hammer, J. and Dohrmann, R. (2020) PE Experiment: Microstructural and mineralogical-geochemical investigations on selected core samples from prospecting boreholes BPE-1, BPE-2 and BPE-3. Mont Terri Technical Note, TN 2018–12, Federal Office of Topography (swisstopo), Wabern, Switzerland.
- Korte, C., Hesselbo, S.P., Ullmann, C.V., Dietl, G., Ruhl, M., Schweigert, G. et al. (2015) Jurassic climate mode governed by ocean gateway. *Nature Communications*, 6(1), 1–7.
- Lauper, B., Jaeggi, D., Deplazes, G. and Foubert, A. (2018) Multi-proxy facies analysis of the Opalinus Clay and depositional implications (Mont Terri rock laboratory, Switzerland). *Swiss Journal of Geosciences*, 111, 383–398.
- Lazar, O.R., Bohacs, K.M., Macquaker, J.H.S., Schieber, J. and Demko, T.M. (2015) Capturing key attributes of fine-grained sedimentary rocks in outcrops, cores, and thin sections: nomenclature and description guidelines. *Journal of Sedimentary Research*, 85, 230–246.
- Lemoine, M., Bas, T., Arnaud-Vanneau, A., Arnaud, H., Dumont, T., Gidon, M. et al. (1986) The continental margin of the Mesozoic

- Tethys in the Western Alps. *Marine and Petroleum Geology*, 3(3), 179–199.
- Lerouge, C., Grangeon, S., Claret, F., Gaucher, E., Blanc, P., Guerrot, C. et al. (2014) Mineralogical and isotopic record of diagenesis from the Opalinus Clay formation at Benken, Switzerland: implications for the modeling of pore-water chemistry in a clay formation. *Clays and Clay Minerals*, 62, 286–312.
- Liniger, L.A. (2016) Entstehung und Zusammensetzung einer Karbonatkonkretion im Opalinuston bei Mont Terri, St. Ursanne (CH). BSc thesis, University of Bern, Bern, Switzerland.
- Lovley, D.R. and Phillips, E.J.P. (1987) Competitive mechanisms for inhibition of sulfate reduction and methane production in the zone of ferric iron reduction in sediments. *Applied and Environmental Microbiology*, 53(11), 2636–2641.
- Löwemark, L., Chen, H.-F., Yang, T.-N., Kylander, M., Yu, E.-F., Hsu, Y.-W. et al. (2011) Normalizing XRF-scanner data: A cautionary note on the interpretation of high-resolution records from organic-rich lakes. *Journal of Asian Earth Sciences*, 40, 1250–1256.
- Mäder, U.K. and Mazurek, M. (1998) Oxidation phenomena and processes in Opalinus Clay: Evidence from the excavation-disturbed zones in Hauenstein and Mt. Terri Tunnels and Siblingen open clay pit. *Materials Research Society Symposia Proceedings*, 506, 731–739.
- Matter, A., Peters, T., Bläsi, H.-R., Meyer, J., Ischi, H. and Meyer, C. (1988) Sondierbohrung Weiach – Geologie. Nagra Technischer Bericht, NTB 86-01, Nagra, Wettingen, Switzerland.
- Matter, A., Peters, T., Isenschmid, C., Bläsi, H.-R. and Ziegler, H.-J. (1987) Sondierbohrung Riniken – Geologie. Nagra Technischer Bericht, Nagra, Wettingen, Switzerland.
- Mazurek, M. (2011) Aufbau und Auswertung der Gesteinsparameter – Datenbank für Opalinuston, den Braunen Dogger, Effinger Schichten und Mergel-Formation des Helvetikums. Nagra Arbeitsbericht, NAB 11-20, Nagra, Wettingen, Switzerland.
- Mazurek, M. and Aschwanden, L. (2020) Multi-scale petrographic and structural characterisation of the Opalinus Clay. Nagra Arbeitsbericht, NAB 19–44, Nagra, Wettingen, Switzerland.
- Mazurek, M. and de Haller, A. (2017) Pore-water evolution and solute-transport mechanisms in Opalinus Clay at Mont Terri and Mont Russelin (Canton Jura, Switzerland). *Swiss Journal of Geosciences*, 110, 129–149.
- Nagra (2001) Sondierbohrung Benken – Untersuchungsbericht. Nagra Technischer Bericht, Nagra, Wettingen, Switzerland.
- Nagra (2002) Projekt Opalinuston: synthese der geowissenschaftlichen Untersuchungsergebnisse. Entsorgungsnachweis für abgebrannte Brennelemente, verglaste hochaktive sowie langlebige mittelaktive Abfälle. Nagra Technischer Bericht, NTB 02-03, Nagra, Wettingen, Switzerland.
- Nagra (2014) SGT Etappe 2: vorschlag weiter zu untersuchender geologischer Standortgebiete mit zugehörigen Standortarealen für die Oberflächenanlage: geologische Grundlagen, Dossier I Einleitung und Zusammenfassung. Nagra Technischer Bericht. Nagra, Wettingen, Switzerland.
- Pearson, F.J., Arcos, D., Bath, A., Boisson, J.-Y., Fernández, A.M., Gäbler, H.-E., Gaucher, E., Gautschi, A., Griffault, L., Hernán, P. and Waber, H.N. (2003) Mont Terri Project – Geochemistry of water in the Opalinus Clay Formation at the Mont Terri Rock Laboratory. Reports of the FOWG, Geology Series, No. 5. Federal Office of Water and Geology, Bern, Switzerland.
- Peters, T. (1962) Tonmineralogische Untersuchungen an Opalinustonen und einem Oxfordienprofil im Schweizer Jura. *Schweizerische mineralogische und petrographische Mitteilungen*, 42, 359–380.
- Price, G.D. (2010) Carbon-isotope stratigraphy and temperature change during the Early-Middle Jurassic (Toarcian-Aalenian), Raasay, Scotland, UK. *Palaeogeography, Palaeoclimatology, Palaeoecology*, 285, 255–263.
- Quenstedt, F.A. (1843) *Das Flözgebirge Württembergs mit besonderer Rücksicht auf den Jura*. Tübingen: Laupp & Siebeck.
- Quenstedt, F.A. (1858) *Der Jura*. Tübingen: Laupp & Siebeck.
- Reineck, H.-E. and Wunderlich, F. (1968) Classification and origin of flaser and lenticular bedding. *Sedimentology*, 11, 99–104.
- Reisdorf, A.G., Hostettler, B., Jaeggi, D., Deplazes, G., Bläsi, H.-R., Morard, A., Feist-Burkhardt, S., Waltschew, A., Dietze, V. and Menkveld-Gfeller, U. (2016) Litho- and biostratigraphy of the 250 m-deep Mont Terri BDB-1 borehole through the Opalinus Clay and bounding formations, St-Ursanne, Switzerland. Mont Terri Technical Report, TR 2016–02, Federal Office of Topography (swisstopo), Wabern, Switzerland.
- Reisdorf, A.G. and Wetzel, A. (2018) Evidence for syndimentary differential tectonic movements in a low-subsidence setting: Early Jurassic in northwestern Switzerland. *Swiss Journal of Geosciences*, 111, 417–444.
- Remane, J., Adatte, T., Berger, J.-P., Burkhalter, R., Dall’Agnolo, S., Decrouez, D. et al. (2005) Richtlinien zur stratigraphischen Nomenklatur. *Eclogae Geologicae Helveticae*, 98(3), 385–405.
- Sandoval, J., O’Dogherty, L., Vera, J.A. and Guex, J. (2002) Sea-level changes and ammonite faunal turnover during the Lias/Dogger transition in the western Tethys. *Bulletin de la Société Géologique de France*, 173(1), 57–66.
- Schieber, J. (2002) The role of an organic slime matrix in the formation of pyritized burrow trails and pyrite concretions. *Palaios*, 17, 104–109.
- Schirardin, J. (1960) Sur la limite du Toarcien et de l’Aalénien en Alsace. *Bulletin du Service de la carte géologique d’Alsace et de Lorraine*, 13(3), 95–126.
- Schmidt, C., Braun, L., Paltzer, G., Mühlberg, M., Christ, P. and Jakob, F. (1924) Die Bohrung von Buix bei Pruntrut und Allschwil bei Basel. Beiträge zur Geologie der Schweiz, Geotechnische Serie, X.
- Siehl, A. and Thein, J. (1989) Minette-type ironstones. *Geological Society, London, Special Publications*, 46(1), 175–193.
- Tardy, Y. and Nahon, D. (1985) Geochemistry of laterites, stability of Al-goethite, Al-hematite, and Fe³⁺-kaolinite in bauxites and ferricretes: an approach to the mechanism of concretion formation. *American Journal of Science*, 285(10), 865–903.
- Taylor, K.G. and Curtis, C.D. (1995) Stability and facies association of early diagenetic mineral assemblages: an example from a Jurassic ironstone-mudstone succession, U.K. *Journal of Sedimentary Research*, A65(2), 358–368.
- Taylor, K.G. and Macquaker, J.H.S. (2011) Iron minerals in marine sediments record chemical environments. *Elements*, 7, 113–118.
- Teyssen, T.A.L. (1984) Sedimentology of the Minette oolitic ironstones of Luxembourg and Lorraine: a Jurassic subtidal sandwave complex. *Sedimentology*, 31, 195–211.
- Teyssen, T. (1989) A depositional model for the Liassic Minette ironstones (Luxemburg and France), in comparison with other Phanerozoic oolitic ironstones. *Geological Society, London, Special Publications*, 46(1), 79–92.
- Thöle, H., Bornemann, A., Heimhofer, U., Luppold, F.W., Blumenberg, M., Dohrmann, R. et al. (2020) Using high-resolution XRF analyses as a sequence stratigraphic tool in a mudstone-dominated succession (Early Cretaceous, Lower Saxony Basin, Northern Germany). *The Depositional Record*, 6(1), 236–258.

- Thury, M. and Bossart, P. (1999) The Mont Terri rock laboratory, a new international research project in a Mesozoic shale formation, in Switzerland. *Engineering Geology*, 52, 347–359.
- Tribouillard, N., Algeo, T.J., Lyons, T. and Riboulleau, A. (2006) Trace metals as paleoredox and paleoproductivity proxies: an update. *Chemical Geology*, 232, 12–32. Blo.
- Turner, B.W., Tréanton, J.A. and Slatt, R.M. (2016) The use of chemostratigraphy to refine ambiguous sequence stratigraphic correlations in marine mudrocks. An example from the Woodford Shale, Oklahoma, USA. *Journal of the Geological Society*, 173(5), 854–868.
- Underhill, J.R. and Partington, M.A. (1993) Jurassic thermal doming and deflation in the North Sea: implications of the sequence stratigraphic evidence. *Geological Society, London, Petroleum Geology Conference Series*, 4(1), 337–345.
- Van Wagoner, J.C., Posamentier, H.W., Mitchum, R.M. Jr, Vail, P.R., Sarg, J.F., Loutit, T.S. and Hardenbol, J. (1988) An overview of the fundamentals of sequence stratigraphy and key definitions. In: Wilgus, C.K., Hastings, B.S., Kendall, C.G.S.C., Posamentier, H.W., Ross, C.A. and Van Wagoner, J.C. (Eds.) *Sea Level Changes – An Integrated Approach. SEPM Special Publication*, 42, 39–45.
- Ver Straeten, C.A., Brett, C.E. and Sageman, B.B. (2011) Mudrock sequence stratigraphy: A multi-proxy (sedimentological, paleobiological and geochemical) approach, Devonian Appalachian Basin. *Palaeogeography, Palaeoclimatology, Palaeoecology*, 304, 54–73.
- Vogel, H., Wagner, B., Zanchetta, G., Sulpizio, R. and Rosén, P. (2010) A paleoclimate record with tephrochronological age control for the last glacial-interglacial cycle from Lake Ohrid, Albania and Macedonia. *Journal of Paleolimnology*, 44, 295–310.
- Wetzel, A., Allenbach, R. and Allia, V. (2003) Reactivated basement structures affecting the sedimentary facies in a tectonically “quiescent” epicontinental basin: an example from NW Switzerland. *Sedimentary Geology*, 157, 153–172.
- Wetzel, A. and Allia, V. (2000) The significance of hiatus beds in shallow-water mudstones: an example from the Middle Jurassic of Switzerland. *Journal of Sedimentary Research*, 70, 170–180.
- Wetzel, A. and Allia, V. (2003) Der Opalinuston in der Nordschweiz: lithologie und Ablagerungsgeschichte. *Eclogae Geologicae Helvetiae*, 96, 451–469.
- Wetzel, A. and Meyer, C.A. (2006) The dangers of high-rise living on a muddy seafloor: an example of crinoids from shallow-water mudstones (Aalenian, northern Switzerland). *Palaios*, 21, 155–167.
- Wildi, W., Funk, H., Loup, B., Amato, E. and Huggenberger, P. (1989) Mesozoic subsidence history of the European marginal shelves of the alpine Tethys (Helvetic realm, Swiss Plateau and Jura). *Eclogae Geologicae Helvetiae*, 82, 817–840.
- Wilson, M.A. and Palmer, T.J. (1992) Hardgrounds and hardground faunas. University of Wales, Aberystwyth, Institute of Earth Studies Publications, 9, 1–131.
- Wohlwend, S., Bläsi, H.-R., Feist-Burkhardt, S., Hostettler, B., Menkveld-Gfeller, U., Dietze, V. et al. (2019) Die Passwang-Formation im östlichen Falten- und Tafeljura: Fasiswald (SO) – Unt. Hauenstein (SO) – Wasserflue (AG) – Thalheim (AG) – Frickberg (AG) – Cheisacher (AG) – Böttstein (AG) – Tegerfelden (AG) – Achberg (AG). Nagra Arbeitsbericht. Nagra, Wettingen, Switzerland.
- Wold, S., Esbensen, K. and Geladi, P. (1987) Principal component analysis. *Chemometrics and Intelligent Laboratory Systems*, 2, 37–52.
- Young, T.P. (1989) Phanerozoic ironstones: an introduction and review. *Geological Society, London, Special Publications*, 46(1), ix–xxv.
- Ziegler, P.A. (1988) Evolution of the Arctic-North Atlantic and the Western Tethys. *AAPG Memoir*, 43, 1–198.
- Ziegler, P.A. (1990) *Geological Atlas of Western and Central Europe*, 2nd ed. London: Shell Internationale Petroleum Mij. B.V. and Geological Society.
- Zimmermann, J., Franz, M., Heunisch, C., Luppold, F.W., Mönnig, E. and Wolgramm, M. (2015) Sequence stratigraphic framework of the Lower and Middle Jurassic in the North German Basin: Epicontinental sequences controlled by Boreal cycles. *Palaeogeography, Palaeoclimatology, Palaeoecology*, 440, 395–416.
- Zimmermann, J., Franz, M., Schaller, A. and Wolgramm, M. (2018) The Toarcian-Bajocian deltaic system in the North German Basin: subsurface mapping of ancient deltas-morphology, evolution and controls. *Sedimentology*, 65, 897–930.

SUPPORTING INFORMATION

Additional supporting information may be found online in the Supporting Information section.

How to cite this article: Lauper B, Deplazes G, Vogel H, et al. Geochemical fingerprinting of key lithologies and depositional processes across the upper boundary of the Opalinus Clay (Aalenian, Middle Jurassic, northern Switzerland). *Depositional Rec* 2020;00:1–27. <https://doi.org/10.1002/dep2.126>